# Buckling of Conventional and High-Strength Vanadium Steel Single- and Double-Angle Compression Members and Truss Subassemblies: Experimental and Computational Correlation Study

AHMET CITIPITIOGLU, MOHAMED M. TALAAT, RONALD L. MAYES, MARK D. WEBSTER, and FRANK W. KAN

## ABSTRACT

High-strength, low-alloy vanadium (HSLA-V) steel offers higher strength and toughness than conventional steel. The resulting lighter weight and more slender structural members are more susceptible to buckling in compression. This study establishes an understanding of buckling in this material and the ability to predict it analytically. A series of conventional ASTM A572 Grade 50 steel and HSLA-V (nominal Grade 80) steel angle compression members were tested at Lehigh University's Advanced Technology for Large Structural Systems (ATLSS) laboratory. A general-purpose finite element (FE) software was used in this study to simulate the buckling and post-buckling behavior of the structural members. The objective of these simulations was to establish confidence in the ability to accurately predict buckling response. The influence of the following modeling parameters on the accuracy of the compression angle member simulation results was investigated: variation in material stress-strain relationship, residual stresses, and the shape and magnitude of geometric imperfections. For the truss subassembly simulations, the influence of the following parameters was also investigated: bracing and boundary element stiffness and design code assumptions of end conditions.

**Keywords:** high-strength vanadium steel, compression, finite element analysis, buckling analysis, geometric imperfection, steel truss.

## INTRODUCTION

Vanadium is a soft, ductile, silver-gray metal, similar in many properties to chromium. It is corrosion-resistant at normal temperature but oxidizes above 600ºC. Vanadium is typically found combined with minerals. In the United States, the primary source of vanadium is spent catalyst from chemical processing plants. Recycling spent catalysts from oil refineries for vanadium reduces or eliminates the need for land-filling up to 6 million pounds of hazardous waste annually. It also reduces energy and waste requirements associated with processing virgin vanadium ores. The principal use of vanadium is in metallic alloys, especially steels. In tool and spring steels, a small amount (less than 1%) adds strength, toughness, and heat resistance. Vanadium compounds are also used in the ceramics, glass, and dye industries and are important as catalysts in the chemical industry. Civil engineering applications include higher strength; lighter, and more ductile, structures, which offer special advantage to resistance of blasts or seismic shocks; as well as large-span and high-rise structures, which mainly support self-weight loads.

The experimental component of this study is based on a laboratory test program carried out in the Advanced Technology for Large Structural Systems (ATLSS) laboratory at Lehigh University. The detailed results of these experimental tests are documented in ATLSS Report No. 08-07, "An Experimental Study on Buckling of Vanadium Steel Members with Single- or Double-Angle Cross-Sections," (Candas et al., 2008). Single- and double-angle members were loaded under monotonic compression loading in the experimental program. The experimental program also included truss subassemblies fabricated using double-angle members and loaded under constant and gradient (moment-couple) loading, both monotonic and cyclic. The full report on this study is documented by Simpson, Gumpertz & Heger Inc. in SGH 2011. A follow-up study is documented in SGH 2012. In SGH 2011, the experimental results were compared to the design equations found in the 2010 AISC *Specifications*

Ahmet Citipitioglu, Director of Engineering and Design, TAV Construction, Istanbul, Turkey. Email: AhmetC@tavc.com.tr

Mohamed M. Talaat, Senior Project Manager, Simpson Gumpertz & Heger Inc., Oakland, Calif. Email: MTalaat@sgh.com (corresponding)

Ronald L. Mayes, Staff Consultant, Simpson Gumpertz & Heger Inc., Oakland, Calif. Email: RLMayes@sgh.com

Mark D. Webster, Senior Consulting Engineer, Simpson Gumpertz & Heger Inc., Waltham, Mass. Email: MDWebster@sgh.com

Frank W. Kan, Principal, Simpson Gumpertz & Heger Inc., Waltham, Mass. Email: FWKan@sgh.com

Paper No. 2017-08R

*for Structural Steel Buildings*, hereafter referred to as the AISC *Specification* (AISC, 2010), and the 2010 "Standard Specification" for open-web steel joists, published by SJI (2010). The purpose of the experimental program was to evaluate the buckling behavior of HSLA-V single- and double-angle members compared to conventional steel members. The research aimed to evaluate the ability to predict the correct failure mode and load capacity for a range of section element local slenderness (width-thickness ratios) and member slenderness ($L/r$ ratios) and to evaluate the effects of end restraint and design assumptions ($K$-factors) on the overall buckling load of constructed subassemblies.

The analytical component of this study consists of FE simulations of experimental angle compression member tests. The objective of these simulations is to establish confidence in the ability to accurately predict buckling response, to investigate the sensitivity of the analytical simulations to a range of modeling and design assumptions, and to identify key modeling parameters and make corresponding recommendations for a subsequent analytical parametric study. Analysis sensitivity to the following parameters was investigated:

- Variability in material stress-strain relationships.
- Residual stresses.
- Magnitude of geometric imperfections.
- Superposition method to obtain initial imperfection shape.
- Member end restraint assumptions.
- Flexibility of boundary elements.

The following section presents a brief review of the treatment of compressive buckling in U.S. design codes.

## TREATMENT OF BUCKLING IN U.S. DESIGN CODES

U.S. design codes use Euler's elastic column buckling equation as its basis to determine compression capacity. This equation is valid for slender members with pinned end conditions:

$$F_{e,i} = \frac{\pi^2 E}{(KL/r)_i^2} \quad \text{where} \quad i = x, y \tag{1}$$

where $F_e$ is the theoretical elastic buckling stress, $E$ is the material's modulus of elasticity, $L$ is the length on the compression member, and $r$ is the radius of gyration of the cross section. Subscript $i$ reflects the two buckling axes: strong and weak axis.

Members with restrained end conditions typically result in higher buckling capacity. For members with differing boundary conditions, the member $L/r$ ratio is modified by an effective length factor, also known as the $K$-factor to define the member slenderness ($KL/r$). The effective length is equal to the distance between inflection points in the compression member where the moment and curvature values are zero (i.e., between "pins") and the member curvature reverses direction. $K$-factors and corresponding effective lengths for various end conditions are shown in Figure 1.

If the compression member's cross-section elements (e.g., column flange, angle leg, etc.) are slender, local buckling of these elements may occur due to local instabilities before the overall member can buckle. Slenderness is related to both the width-to-thickness ($b/t$) ratio of the member cross-section elements (e.g., of the angle leg) and the material strength. This determines whether the section is a nonslender-element or a slender-element section. In nonslender-element sections, local buckling will occur long after the section has yielded; in slender-element sections, local buckling will occur before yielding and significantly reduce the compression member capacity. For members subject to flexure, sections are classified as compact, noncompact, or slender-element sections.

### Members with Slender Elements

The AISC treatment of compression members with slender elements has changed with the 2016 AISC *Specification* (AISC, 2016). In previous AISC *Specifications*, the effect of element slenderness was accounted for according to the section geometry and considered to be independent of the stress level at which buckling occurs.

The 2010 AISC *Specification* defines a slenderness reduction factor, $Q$, that is introduced into the buckling equations as a multiplier to the material yield strength. The more slender the compression member cross-section elements (greater $b/t$ ratio), the lower the $Q$-factor value, which typically ranges from 1.0 to 0.7. Figure 2 shows the slenderness reduction factor equations for angles. The current SJI Specification (SJI, 2020) uses the AISC 2010 *Specification* approach to determine the compressive buckling strength for members with slender elements.

The 2016 AISC *Specification* defines an effective area of the element cross section to account for element slenderness while calculating the member compressive strength. This effective area is based on the summation of the effective widths. For slender angle elements, the effective width for each leg is determined based on the width-to-thickness ratio, $\lambda$, with respect to the limiting width-to-thickness ratio, $\lambda_r$, which is defined as $\lambda_r = b/t = 0.45\sqrt{E/F_y}$ for

angles. Figure 3 shows the effective width equations for angles.

### Flexural Buckling Strength

The member compression flexural buckling strength is calculated by determining the critical buckling stress. The change in the critical stress in relation to the member slenderness is shown in Figure 4. "Elastic buckling" occurs when slender compression members buckle at stresses lower than the material's elastic limit. It is characterized by the ability of the buckled compression member to regain its initial shape once the load is removed. On the other hand, "inelastic buckling" occurs when less slender members develop plastic deformations prior to reaching their buckling capacities. This results in unrecoverable permanent deformations.

The 2010 AISC *Specification* and the 2020 SJI Specification calculate the nominal compressive flexural buckling strength as follows:

$$P_n = F_{cr}A_g \tag{2}$$

The critical flexural buckling stress including slenderness effects, $F_{cr}$, is calculated as follows:

$$\text{when } \left(\frac{KL}{r}\right)_i \le 4.71\sqrt{\frac{E}{QF_y}} \quad \left(or \quad \frac{QF_y}{F_e} \le 2.25\right)$$

$$F_{cr} = \left(0.658^{\frac{QF_y}{F_{e,i}}}\right)QF_y \tag{3}$$

$$\text{when } \left(\frac{KL}{r}\right)_i > 4.71\sqrt{\frac{E}{QF_y}} \quad \left(or \quad \frac{QF_y}{F_e} > 2.25\right)$$

$$F_{cr} = 0.877F_{e,i} \tag{4}$$

where $A_g$ is the section gross area, $F_e$ is the theoretical elastic buckling stress given in Equation 1, $Q$ is the slenderness reduction factor for compression members with slender cross-section elements shown in Figure 2, and $(KL/r)_i = 4.71\sqrt{E/QF_y}$ demarcates elastic and inelastic buckling.

The 2016 AISC *Specification* calculates the nominal compressive flexural buckling strength as follows:

$$P_n = F_{cr}A_e \tag{5}$$

The critical flexural buckling stress, $F_{cr}$, is calculated as follows:

$$\text{when } \left(\frac{KL}{r}\right)_i \le 4.71\sqrt{\frac{E}{F_y}} \quad \left(\text{or } \frac{F_y}{F_e} \le 2.25\right)$$

$$F_{cr} = \left(0.658^{\frac{F_y}{F_{e,i}}}\right)F_y \tag{6}$$

$$\text{when } \left(\frac{KL}{r}\right)_i > 4.71\sqrt{\frac{E}{F_y}} \quad \left(\text{or } \frac{F_y}{F_e} > 2.25\right)$$

$$F_{cr} = 0.877F_{e,i} \tag{7}$$

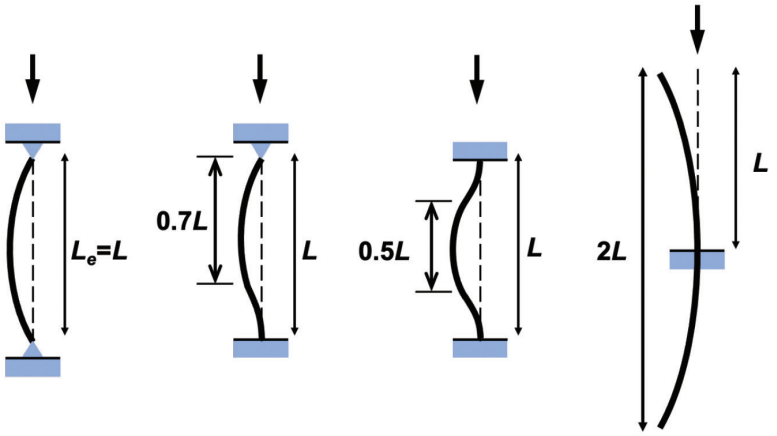


| Boundary Condition | Pinned-Pinned | Fixed-Pinned | Fixed-Fixed | Fixed-Free* |
|---|---|---|---|---|
| Effective Length | *L* | 0.7*L* | 0.5*L* | 2*L* |
| *K*-factor | 1.0 | 0.7 | 0.5 | 2.0 |

* The Fixed-Free column is "mirrored" through the fixed end to visualize $L_e$=2*L*

*Fig. 1. Effective length factor,* K, *for typical member end conditions.*

This is the same relation given in Equations 3 and 4 without the slenderness reduction factor, $Q$. The determination of the effective member cross section area, $A_g$, to account for slenderness is shown in Figure 3.

**Built-Up Members**

Compression strength of members built up from two or more shapes interconnected by bolted or welded elements are influenced by the stiffness and relative displacement of the connectors between the individual shapes forming the member. In both versions of the AISC *Specifications* (2010, 2016) and the 2020 SJI Specification, the slenderness ratio about the major axis is modified as follows for double angles:

when $a/r_i \le 40$

$$\left(\frac{L_c}{r}\right)_m = \left(\frac{L_c}{r}\right)_y \tag{8}$$

when $a/r_i > 40$

$$\left(\frac{L_c}{r}\right)_m = \sqrt{\left(\frac{L_c}{r}\right)_y^2 + \left(\frac{0.5a}{r_i}\right)^2} \tag{9}$$

where $a$ is distance between connectors along the length of the member and $r_i$ is the minimum radius of gyration for a single angle. The definition of local axes in double-angle member cross sections is shown in Figure 5. The effective length of the built-up member, $L_c$, is equivalent to $KL$: the effective length factor, $K$, times the unbraced length, $L$. It

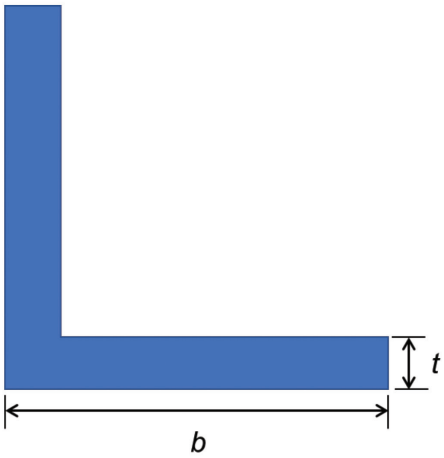


$$\text{when } \frac{b}{t} \le 0.45\sqrt{\frac{E}{F_y}}$$

$$Q_s = 1.0$$

$$\text{when } 0.45\sqrt{\frac{E}{F_y}} < \frac{b}{t} \le 0.91\sqrt{\frac{E}{F_y}}$$

$$Q_s = 1.34 - 0.76\left(\frac{b}{t}\right)\sqrt{\frac{F_y}{E}}$$

$$\text{when } \frac{b}{t} < 0.91\sqrt{\frac{E}{F_y}}$$

$$Q_s = \frac{0.53E}{F_y(b/t)^2}$$

*Fig. 2. Reduction factor,* Q*, for angles per AISC* Specification *(2010).*

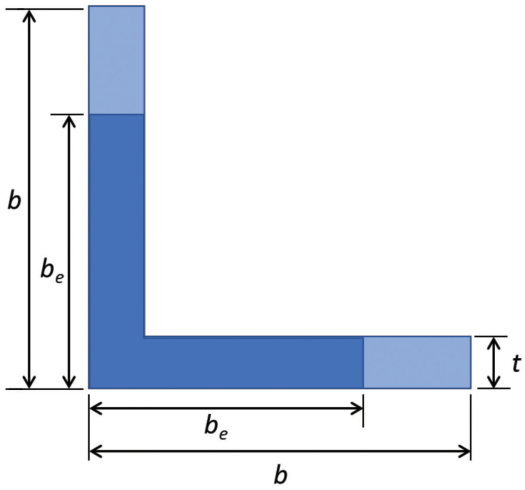


$$\text{when } \lambda \le \lambda_r\sqrt{\frac{F_y}{F_{cr}}}$$

$$b_e = b$$

$$\text{when } \lambda > \lambda_r\sqrt{\frac{F_y}{F_{cr}}}$$

$$b_e = b\left(1 - c_1\sqrt{\frac{F_{el}}{F_{cr}}}\right)\sqrt{\frac{F_{el}}{F_{cr}}}$$

*Fig. 3. Effective width,* $b_e$*, for angles per AISC* Specification *(2016).*

is worth noting that the different modification factors given in the 2005 and 2010 AISC *Specifications* were evaluated in SGH (2011) and concluded that using either modification factor results in similarly better correlation with experimental results than not using either.

For built-up (i.e., double-angle) compression members, both versions of the AISC *Specification* (2010 and 2016) and of the SJI Specifications (2010 and 2020) apply the flexural buckling equation about both member axes, and the lower critical buckling stress governs the overall member strength. The AISC *Specifications* also consider the flexural-torsional buckling strength, which is not considered by the SJI Specifications.

**Flexural Torsional Buckling Strength**

The 2016 AISC *Specification* calculates the nominal compressive flexural-torsional buckling strength for double angles as follows:

$$P_n = F_{cr} A_e \tag{10}$$

where the critical stress, $F_{cr}$, is determined using Equations 6 and 7 with the elastic buckling stress, $F_e$, calculated using the following equations. The calculation of $A_e$ is shown Figure 3.

$$F_e = \frac{F_{ey} + F_{ez}}{2H}\left[1 - \sqrt{1 - \frac{4F_{ey}F_{ez}H}{\left(F_{ey} + F_{ez}\right)^2}}\right] \tag{11}$$

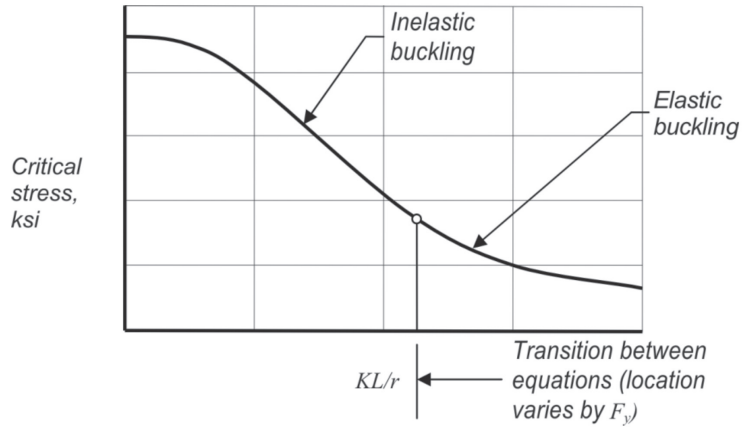


*Fig. 4. Standard flexural buckling critical stress curve.*

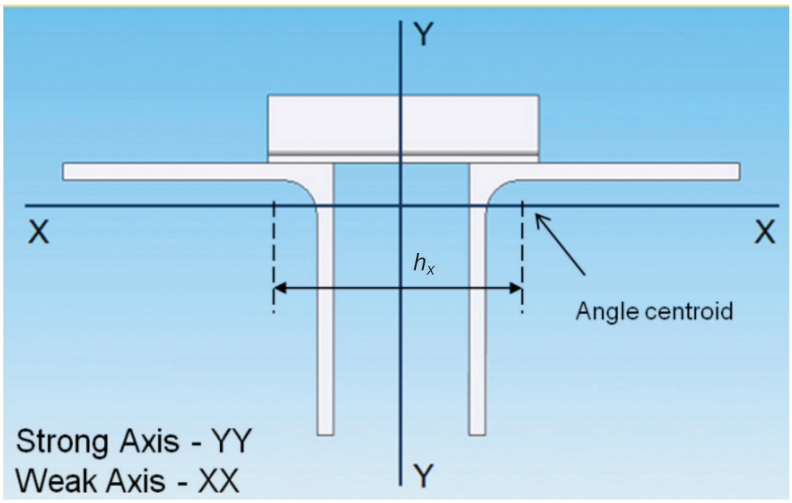


*Fig. 5. Definition of local axes in double-angle member cross section.*

$$F_{ez} = \frac{GJ}{A\bar{r}_o^2} \tag{12}$$

$$H = 1 - \frac{x_o^2 + y_o^2}{\bar{r}_o^2} \tag{13}$$

$$\bar{r}_o^2 = x_o^2 + y_o^2 + \frac{I_x + I_y}{A_g} \tag{14}$$

$$J = \frac{At^3}{3} \tag{15}$$

where $F_{ey}$ is the elastic buckling stress about the strong axis ($y$-axis) calculated using Equation 1, including the modified member slenderness of Equations 8 and 9; $J$ is the torsional moment of inertia; $A$ is the double angle cross-sectional area; $t$ is the angle leg thickness; $G$ is the shear modulus of elasticity; $x_o$ and $y_o$ are the distances from the composite centroid to the angle shear center; and $\bar{r}_o$ is the polar radius of gyration about the double-angle section shear center.

### Governing Buckling Strength

Due to the additional flexural-torsional buckling provisions mentioned previously, the AISC *Specifications* can result in more conservative estimates of buckling strength than the SJI Specifications. The nominal buckling load strength to member slenderness, $L/r$, curves calculated using both SJI (SJI, 2020) and the AISC *Specification* (AISC, 2016) are compared for double-angle cross section members with and without slender section elements in Figures 6 and 7, respectively. These curves are calculated for the member end conditions pinned about the strong axis and fixed about the weak axis and for the two angles connected by a single spacer element. The following buckling modes are calculated:

- Sum of the nominal buckling strength of the two individual single angles over the unbraced length between spacers, $P_{n-L\,flex\,z}$.
- Nominal double-angle flexural buckling strength about both weak and strong axis, $P_{n-LL\,flex\,x}$ and $P_{n-LL\,flex\,y}$.

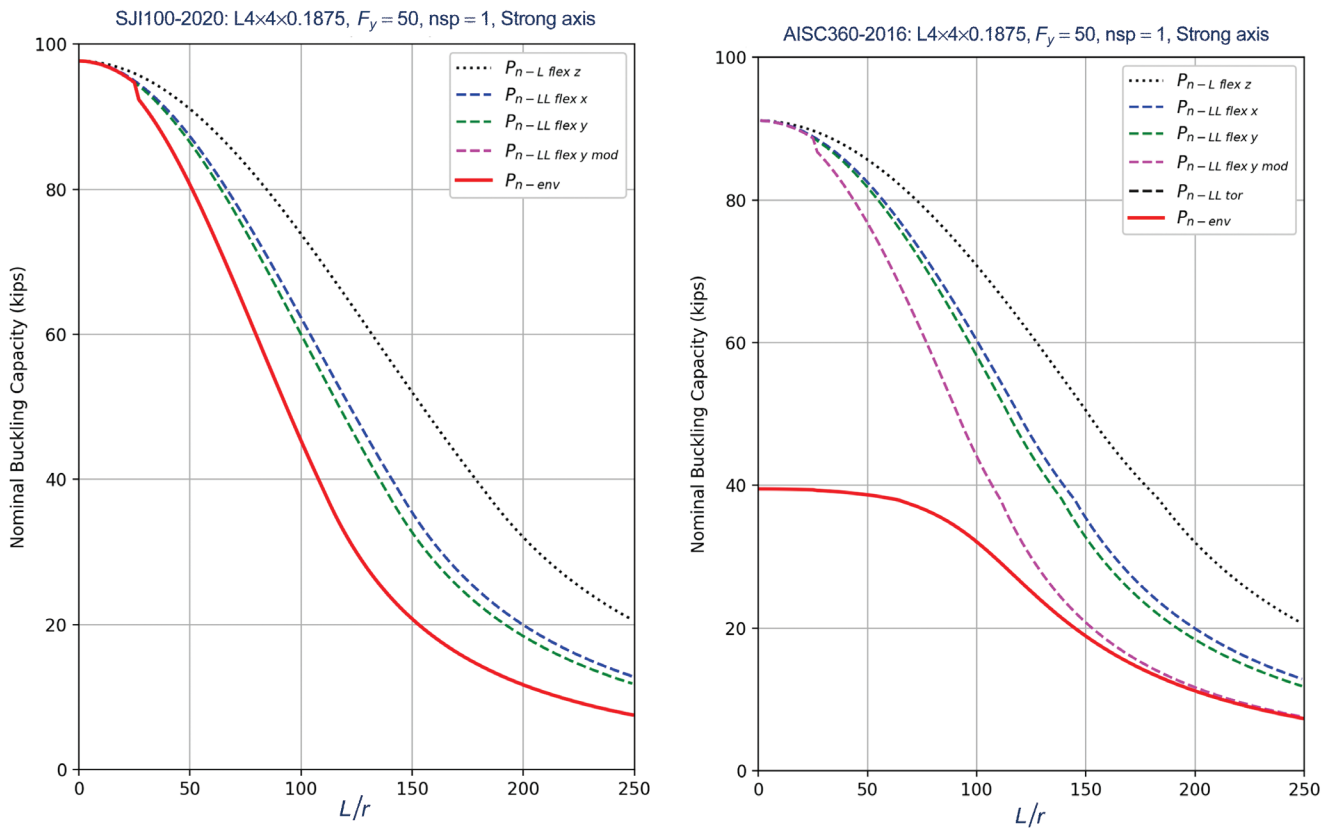


*(a) 2020 SJI 100* (Q = 0.7) *(b) AISC 2016* Specification ($A_e$ = 0.62A *to* 0.95A)

*Fig. 6. Example multi-mode nominal buckling strength curves for double-angle members with slender section elements.*

- Nominal double-angle flexural buckling strength with the modified member slenderness ratio, which accounts for the influence of the connector between the angles, $P_{n-LL\ flex\ y\ mod}$. (The kink in the curve at low $L/r$ values is due to the change in conditions that dictate using Equation 8 instead of Equation 9.)
- Nominal double-angle flexural-torsional buckling strength per the 2016 AISC *Specification* (AISC, 2016), $P_{n-LL\ tor}$.

The solid red line represents the lower-bound nominal strength envelope, $P_{n-env}$, of all the buckling modes listed.

### Effect of Residue Stresses and Initial Imperfections

The critical buckling stress within the inelastic buckling range (Figure 4) is sensitive to residual stresses and initial imperfections. Galambos (1998) compares experimental tests and AISC critical load estimates for flexural buckling of I-shaped columns, which suggests that a larger spread of experimental results from the analytical prediction takes place in the inelastic buckling range. Adluri and Madugula (1996) measured residual stress distributions in angle specimens, which reflect a wide dispersion within the cross section (Figure 8). Design equations typically account for the effects of residual stresses and initial imperfections empirically. In analytical studies, these effects need to be properly accounted for in the simulation models in order to obtain accurate results.

## REVIEW OF EXPERIMENTAL PROGRAM

The analytical studies make use of a two-part experimental study: tests of individual compression single- and double-angle compression members and tests on truss subassemblies. The test programs are reviewed in the following sections.

### Single- and Double-Angle Compression Member Tests

The size, length, nominal strength, compactness, slenderness ratios, and experimental buckling loads for the 6 single-angle compression test specimens are listed in Table 1. The same properties, with the addition of the

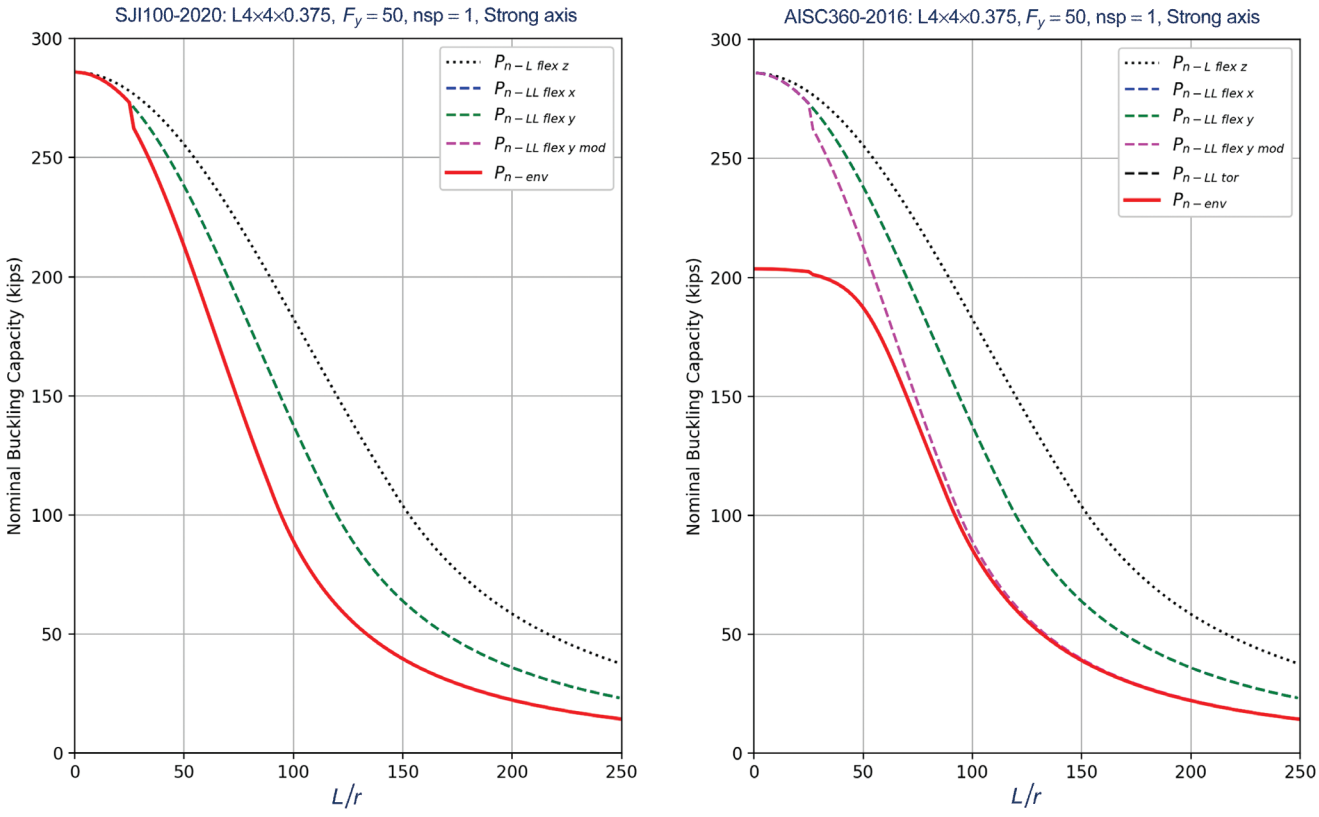


*(a) 2020 SJI100 (Q = 1)*

*(b) AISC 2016 Specification ($A_e$ = A)*

*Fig. 7. Example multi-mode nominal buckling strength curves for double-angle members without slender section elements. [Note that the two curves for $P_{n-LL\ flex\ x}$ and $P_{n-LL\ flex\ y}$ are overlapping in the plots as $(L_{cx}/r_x) = (L_{cy}/r_y)$ for this member section.]*

| Table 1. Single-Angle Test Variables | | | | | | |
|---|---|---|---|---|---|---|
| Test No. | Size | Material | Length (in.) | *Q* | *L*/*r* | Buckling Load (kips) |
| SA1 | L3.5×3.5×⅜ | 80 ksi | 24 | 0.97 | 18 | 188 |
| SA2 | L3.5×3.5×⅜ | 80 ksi | 50 | 0.97 | 44 | 162 |
| SA3 | L3.5×3.5×⅜ | 50 ksi | 24 | 1.00 | 18 | 159 |
| SB1 | L3×3×3/16 | 80 ksi | 24 | 0.70 | 20 | 67.7 |
| SB2 | L3×3×3/16 | 80 ksi | 48 | 0.70 | 40 | 56.6 |
| SB3 | L3×3×3/16 | 50 ksi | 24 | 0.83 | 20 | 55.9 |

number of spacers, are listed for the 20 double-angle compression test specimens in Table 2.

Of the total of 26 compression specimens, 21 were fabricated using HSLA-V material, with a nominal 80-ksi yield stress, while the remaining 5 specimens were of Grade 50 steel material (test results for specimen DC5 were not reported). For all tests, the range of weak-axis member slenderness ratios, *L*/*r*, varied from 18 to 102, and slenderness reduction factors, *Q*, ranged from 0.7 to 1.0. For the double-angle members tested, DA test series double angles were spaced 1 in. apart, while DB and DC test series double angles were spaced 1.5 in. apart. Spacers are used to control the flexural failure of a single angle prior to the flexural buckling strength of the member as a whole.

The test setup used cylindrical bearings, which allowed rotation about the strong axis while restraining rotation about the weak axis. Thus, the *K*-factor for weak-axis flexural buckling for all the test specimens is 0.5.

Tensile yield tests performed on coupons taken from the tested specimens show variabilities in the stress-strain response. Figure 9 shows plots of the individual coupon test results, for L3.5×3.5×⅜ angle size, and the best-fit curve used in the FE analyses.

The average measured out-of-straightness imperfection magnitude of the tested specimens was *L*/1514, where *L* is the nominal specimen length.

### Truss Subassembly Tests

The truss subassembly tests performed at Lehigh (Candas et al., 2008) included two different types of tests: constant moment (CM) tests and gradient moment (GM) tests. Only the CM test setup, shown schematically in Figure 10(a), is addressed in this study. The CM test setup is intended to evaluate the performance near the truss midspan, where the bending moment is high and the shear is low. The specimens were loaded with a moment couple [Figure 10(b)].

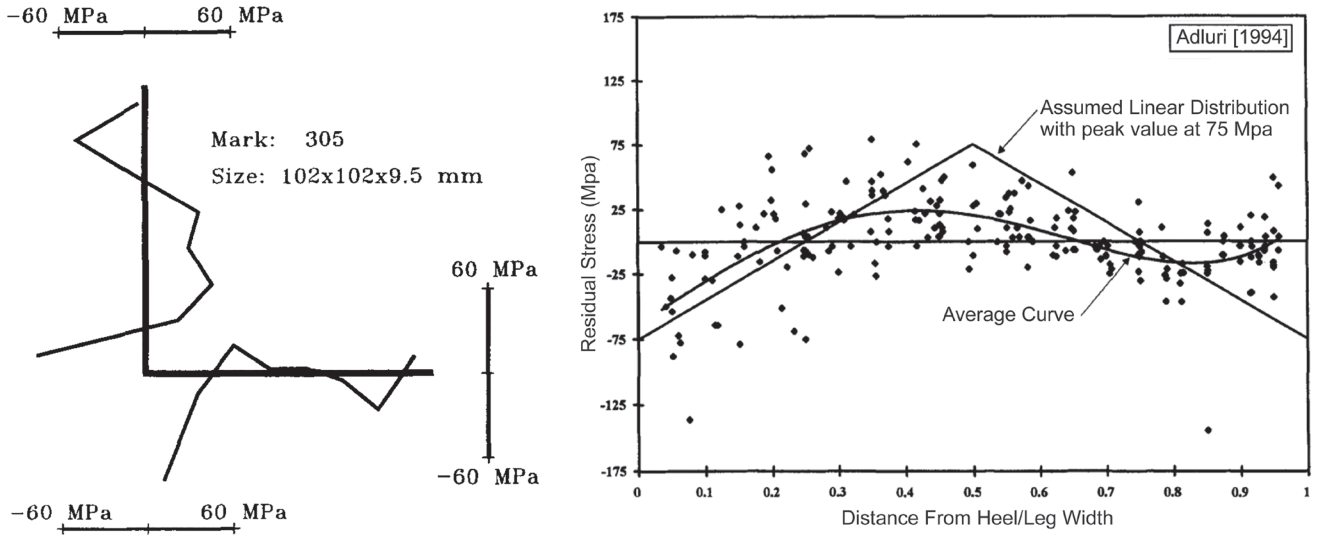


*(a) Sample distribution in cross section*

*(b) Measured and fitted values across angle leg*

*Fig. 8. Measurements and idealizations of residual stresses in steel angles (Adluri and Madugula, 1996).*

| Table 2. Double-Angle Test Variables | | | | | | | |
|---|---|---|---|---|---|---|---|
| **Test No.** | **Size** | **Number of Spacers** | **Material** | **Length (in.)** | ***Q*** | ***L*/*r*** | **Buckling Load (kips)** |
| DA1 | LL3.5×3.5×⅜ | 2 | 80 ksi | 30 | 0.970 | 28 | 361 |
| DA12 | LL3.5×3.5×⅜ | 2 | 80 ksi | 30 | 0.970 | 28 | 360 |
| DA2 | LL3.5×3.5×⅜ | 2 | 80 ksi | 48 | 0.970 | 45 | 344 |
| DA22 | LL3.5×3.5×⅜ | 2 | 80 ksi | 48 | 0.970 | 45 | 362 |
| DA3 | LL3.5×3.5×⅜ | 2 | 80 ksi | 66 | 0.970 | 61 | 342 |
| DA4 | LL3.5×3.5×⅜ | 2 | 80 ksi | 84 | 0.970 | 78 | 339 |
| DA42 | LL3.5×3.5×⅜ | 2 | 80 ksi | 84 | 0.970 | 78 | 301 |
| DA5 | LL3.5×3.5×⅜ | 2 | 50 ksi | 48 | 1.00 | 45 | 314 |
| DB1 | LL3×3×3⁄16 | 2 | 80 ksi | 24 | 0.700 | 26 | 143 |
| DB2 | LL3×3×3⁄16 | 2 | 80 ksi | 48 | 0.700 | 51 | 127 |
| DB3 | LL3×3×3⁄16 | 2 | 80 ksi | 72 | 0.700 | 77 | 118 |
| DB4 | LL3×3×3⁄16 | 2 | 80 ksi | 96 | 0.700 | 102 | 86.2 |
| DB5 | LL3×3×3⁄16 | 2 | 50 ksi | 48 | 0.830 | 51 | 99.1 |
| DC1 | LL1.75×1.75×⅛ | 3 | 80 ksi | 24 | 0.780 | 44 | 63.6 |
| DC2 | LL1.75×1.75×⅛ | 3 | 80 ksi | 33 | 0.780 | 60 | 58.4 |
| DC3 | LL1.75×1.75×⅛ | 3 | 80 ksi | 42 | 0.780 | 77 | 52.3 |
| DC32 | LL1.75×1.75×⅛ | 3 | 80 ksi | 42 | 0.780 | 77 | 47.3 |
| DC4 | LL1.75×1.75×⅛ | 3 | 80 ksi | 51 | 0.780 | 94 | 47.9 |
| DC42 | LL1.75×1.75×⅛ | 3 | 80 ksi | 51 | 0.780 | 94 | 42.5 |
| DC5[a] | LL1.75×1.75×⅛ | 3 | 50 ksi | 24 | 0.900 | 44 | NA |

[a] Results not reported in Candas et al. (2008).

| Table 3. Truss Subassembly Member and Weld Sizes | | | |
|---|---|---|---|
| **Member Type** | **Size** | **Yield/Ultimate Stress (ksi)** | **Web-to-Chord Fillet Weld (in.)** |
| Chord | LL3.5×3.5×⅜ | 73.7/97.5 | NA |
| Diagonal web | LL1.75×1.75×⅛ | 78.5/101 | ⅛ (⅛) |
| Vertical web | LL1×1×⅛ | 60.2/83.4 | ⅛ (⅛) |
| Vertical web at loaded end | LL2×2×3⁄16 | 76.9/100 | NA (3⁄16) |

The truss assemblies consisted of three panels each and were tested in a horizontal position. The panel points P3 and P5 were braced against truss out-of-plane buckling. The bracing detail is shown in Figure 10(c). The dominant failure mode of the CM specimens was buckling of the compression chord in the relatively longer middle panel. The three-dimensional displacement responses measured at the double-angle mid-spacers were recorded at working points P2, P4, and P6, as shown in Figure 10(a). Initial imperfections were not measured prior to testing.

Table 3 lists the truss subassembly member sizes and material strengths determined from coupon tests. Table 4 describes the differences between the truss specimen configurations. Specimens C1 through C3 were tested under a monotonic load application until the West chord buckled. Specimens C4 and C5 were loaded in one direction until the West chord buckled (Phase 1), unloaded (Phase 2), and then subjected to a reversed load application until the East chord buckled (Phase 3). Phase 1 and Phase 3 loading refer to loading regimes causing buckling in the West and East chords, respectively.

### Main Observations

The major experimental test findings reported in SGH 2011 are summarized as follows:

- The post-buckling deformed shapes of both individual single- and double-angle test specimens included both flexural and torsional modes, but it is not clear whether the buckling initiated as flexural-torsional or flexural

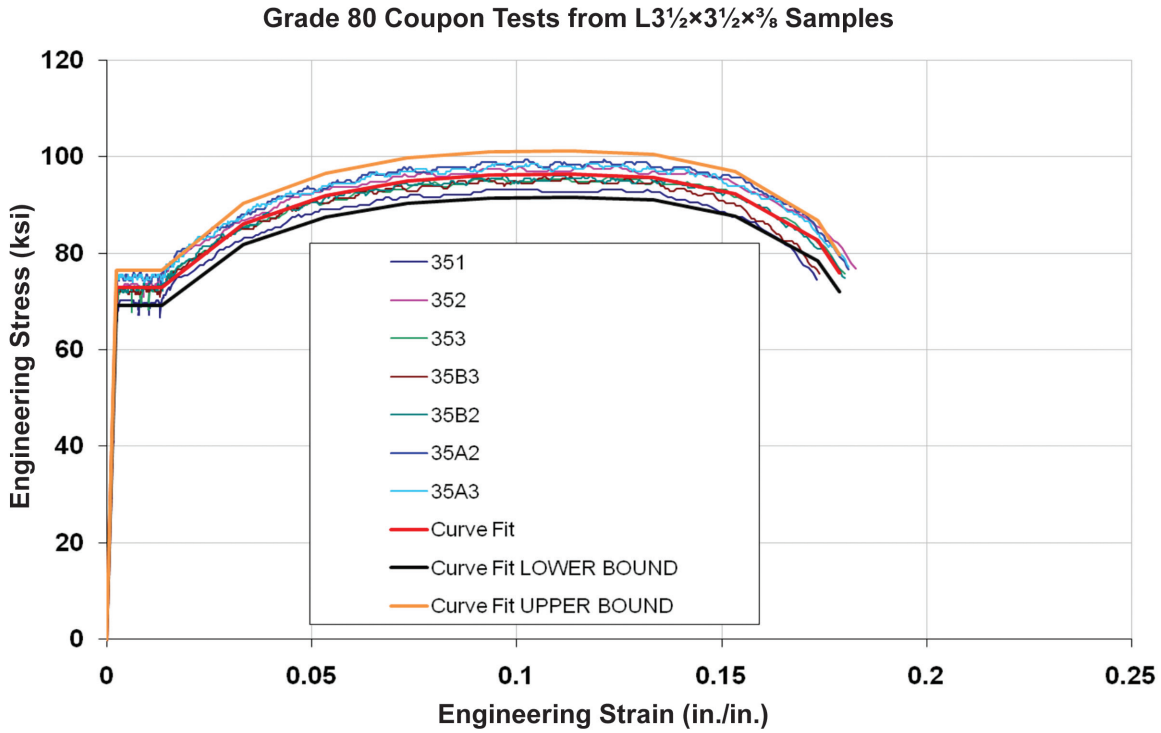


*Fig. 9. Material stress-strain response from coupon tests compared to curve-fitted relationship used in FE analyses.*

| Table 4. Truss Subassembly Specimen Information | | | |
|---|---|---|---|
| **Spec.** | **Number of Spacers** | **Description** | **Observed Buckling Mode and Location** |
| C1 | 3 | Base case, designed per SJI procedures | Out of plane, Middle, and North panels |
| C2 | 3 | Remove vertical web members to permit chord in-plane buckling | In-plane, North panel |
| C3 | 3 | Use rotational restraints at panel points | Out of plane, Middle panel |
| C4 | 1 | Use fewer chord-spacers | Out of plane, Middle panel |
| C5 | 5 | Use more chord-spacers | Out of plane, Middle panel |

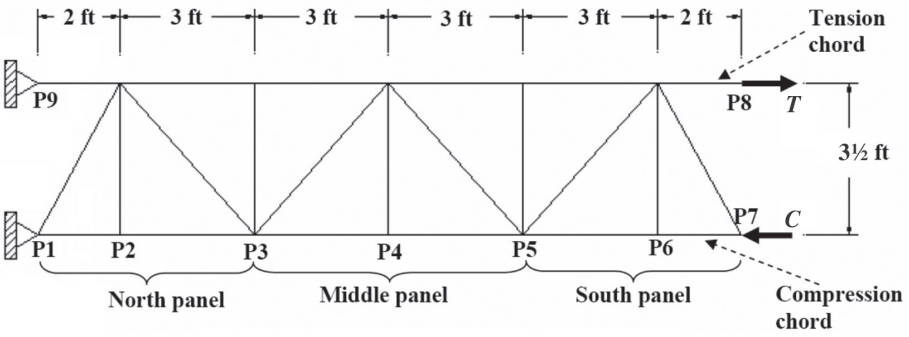


*(a) Structural system and dimensions*

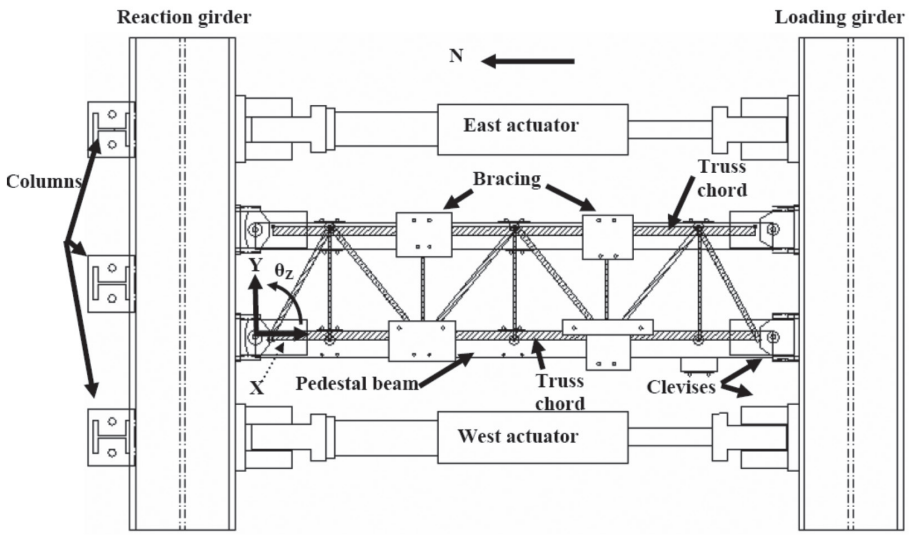


*(b) Test setup*

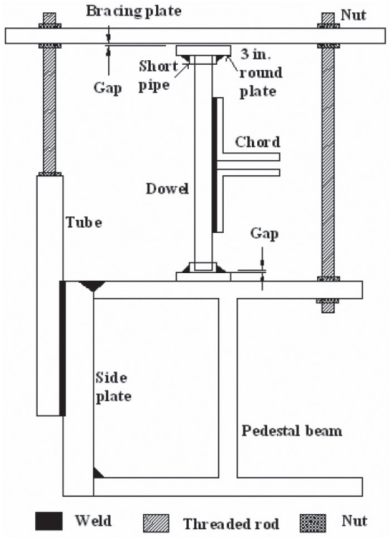


*(c) Chord bracing detail*

*Fig. 10. Truss subassembly-constant moment (CM) test (Candas et al., 2008).*

buckling. The measured capacities of the specimens were in closer agreement with the AISC-predicted flexural buckling strength about the strong axis (i.e., *y*-axis).

- The 2010 AISC *Specification* was significantly more conservative in predicting the strength of test specimens with smaller $Q$-values (more slender angle legs) than in predicting the strength of specimens with larger $Q$-values.
- The buckling strengths predicted using the 2010 AISC *Specification* were equally conservative for both the individual double-angle test specimens and the double-angle members in the truss subassemblies.

## COMPUTATIONAL SIMULATION OF SINGLE- AND DOUBLE-ANGLE MEMBERS

### FE Model Description and Analytical Sensitivity Study Matrix

The computational simulation software ABAQUS (2007) was used in this study. The FE models used four-node shell elements for the angle surfaces and eight-node continuum elements for bar spacers in modeling the double-angle specimens. A preliminary mesh sensitivity study concluded that the use of ~0.15-in. element size was sufficient to capture the displacement modes. The model boundary conditions reproduced those in the experimental setup. The load was applied by displacement control using the arc-length method (also called the Modified Riks algorithm) available in ABAQUS for loading regimes with geometrically unstable phases.

#### *Sensitivity to Material Response*

The modeling of the single- and double-angle specimens and investigation of sensitivity to modeling parameters was initiated by establishing a base-case geometry for each specimen. The base case was constructed using imperfections measured in the laboratory and interpolated by splines to create fitted surfaces along the specimen length. The best-fit material stress-strain curve shown in Figure 9 was used in the base-case analyses. (The stress-strain curve was converted to true stress-strain quantities to satisfy ABAQUS input requirements.)

The sensitivity to variability in the material stress-strain relationship was investigated by constructing two additional simulation cases for each specimen. These cases used the base-case geometry but adopted lower- and upper-bound stress-strain relationships obtained by multiplying the best-fit response by 0.95 and 1.05, respectively (Figure 9). The base-case simulation results compared to those using the upper- and lower-bound material response curves are listed in Tables 5 and 9 for single and double angles, respectively.

#### *Sensitivity to Initial Imperfection*

The sensitivity to initial imperfection was investigated by constructing 12 additional simulation cases for each specimen. First, a geometrically perfect model was constructed from nominal geometry. An elastic buckling analysis was used to compute the buckling loads and shapes. Geometric imperfections were introduced by combining a number of buckling mode shapes that fall within a given multiple of the fundamental elastic load and scaling them so that the maximum imperfection magnitude meets a specified target. Example imperfect shapes are shown in Figure 11 for a short single-angle specimen and in Figure 12 for a slender double-angle specimen. The sensitivity study matrix included the following variables:

- Maximum imperfection magnitude: $L/500$ and $L/1500$. $L/1500$ is the assumption used in developing code equations. $L/500$ is used to investigate the effects of lower manufacturing quality control.
- Number of mode shapes to superimpose: modes within 2, 5, and 10 times the elastic buckling load, $F_b$.
- Combination of mode shapes: superimposed uniformly and inversely proportional to elastic buckling loads.

These results are listed in Tables 6 and 7 for single angles and Tables 10 and 11 for double angles.

#### *Sensitivity to Residual Stress*

The sensitivity to residual stresses was investigated by constructing six additional simulation cases for each specimen. An initial imperfection magnitude of $L/1500$, distributed using inversely proportional weights of mode shapes within twice the elastic buckling load was assigned to these six simulations. The number of shell element strips per angle leg was set to 20 in order to obtain a fixed resolution of the residual stress distribution. The residual stress was imposed as an initial load step. The sensitivity study matrix included the following variables:

- Maximum residual stress magnitude: $0.2F_y$ and $0.3F_y$.
- Residual stress profile: symmetric, half-symmetric, and asymmetric (Figure 13). These profiles are referred to in the results as "all," "half," and "v," respectively. These profiles are intended to bound the wide dispersion of data reported in (Adluri and Madugula, 1996).

These results are listed in Tables 8 and 12 for single and double angles, respectively.

## Discussion of Results

The experimental and analytical initial stiffness, peak load, buckling mode, and post-buckling behavior were examined for each specimen. On average, the analytical initial stiffness was slightly higher than the experimental value. The analytical peak loads for the base cases (Tables 5 and 9) were higher for all L3½×3½×⅜ and L1¾×1¾×⅛ angle tests, and lower for most L3×3×3⁄16 angle tests. The reasons for this pattern are not evident. The differences between analytical and experimental capacities were larger for specimens with higher slenderness. The analytical deformed shapes were in agreement with those observed in the laboratory tests, suggesting that the underlying mechanisms leading to buckling are captured. The analytical post-buckling behavior was generally in agreement with laboratory observations, although the softening curve exhibited a more sharply descending shape just after the peak load, which is common in such numerical simulations due to numerical localization of inelasticity and the absence of a physical loading mechanism (hydraulics, control, etc.) in the simulation. Figure 14 illustrates the comparison for specimen DA22.

Figure 15 shows the effect of analytically generated

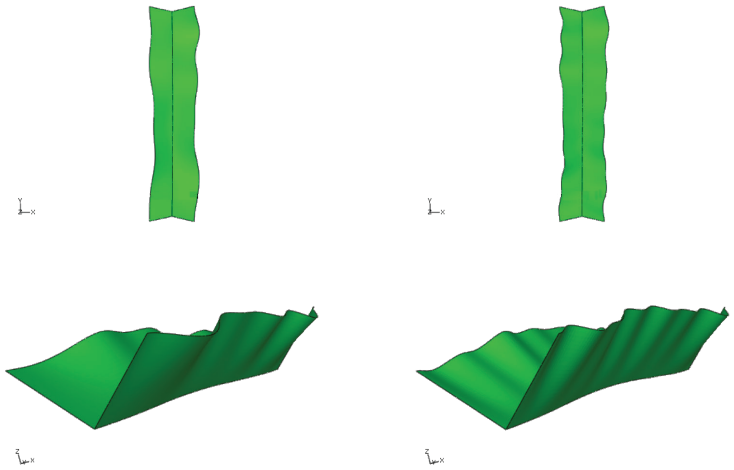

*(a)* 5$F_b$ *(b)* 10$F_b$

*Fig. 11. Generated (magnified) geometric imperfection shapes of Specimen SA1 using uniform weights for modes within 5 and 10 times the elastic buckling load.*

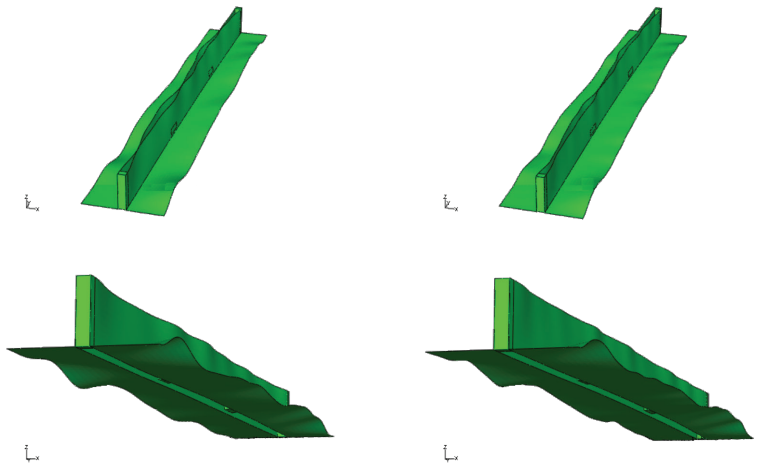

*(a)* 5Fb *(b)* 10Fb

*Fig. 12. Generated (magnified) geometric imperfection shapes of Specimen DA22 using inversely proportionate weights for modes within 5 and 10 times the elastic buckling load.*

imperfections on the buckling response for specimen DA22. Comparing plots (a) and (b) suggests that the effect of the mode combination method is not significant for this specimen. In both plots, the base cases have analytical buckling loads (capacities) higher than the experimental values. The cases with analytically generated imperfections all have closer-matching capacities equal to or smaller than the experimental values. The sensitivity to the maximum imperfection magnitude and number of modes are within 5%.

Figure 16 shows the effect of residual stresses for specimen DA22. For this specimen, the cases with residual stress modeled all have closer-matching capacities equal to or smaller than the experimental values. The sensitivity to the different residual stress profile is small.

The analytical buckling loads from all simulations are summarized in Tables 5 to 8 (for single-angle specimens) and Tables 9 to 12 (for double-angle specimens). The following provides a summary of the analytical results:

- The ratio of analytical to experimental buckling loads for the single-angle base cases ranges from 0.86 to 1.11 (Table 5), with an average of 0.99. For double-angle specimens, the range is 0.90 to 1.17, with an average of 1.07 (Table 9).

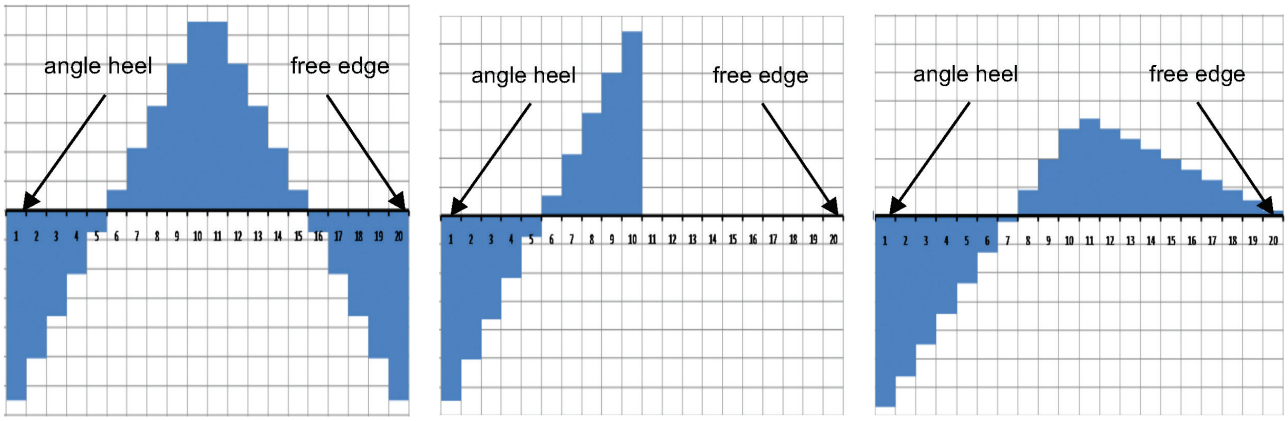


*(a) Full symmetric [all]* *(b) Half symmetric [half]* *(c) Asymmetric [v]*

*Fig. 13. Residual stress profiles across the angle leg. Vertical axis is the relative residual stress magnitude; positive residual stress is tension.*

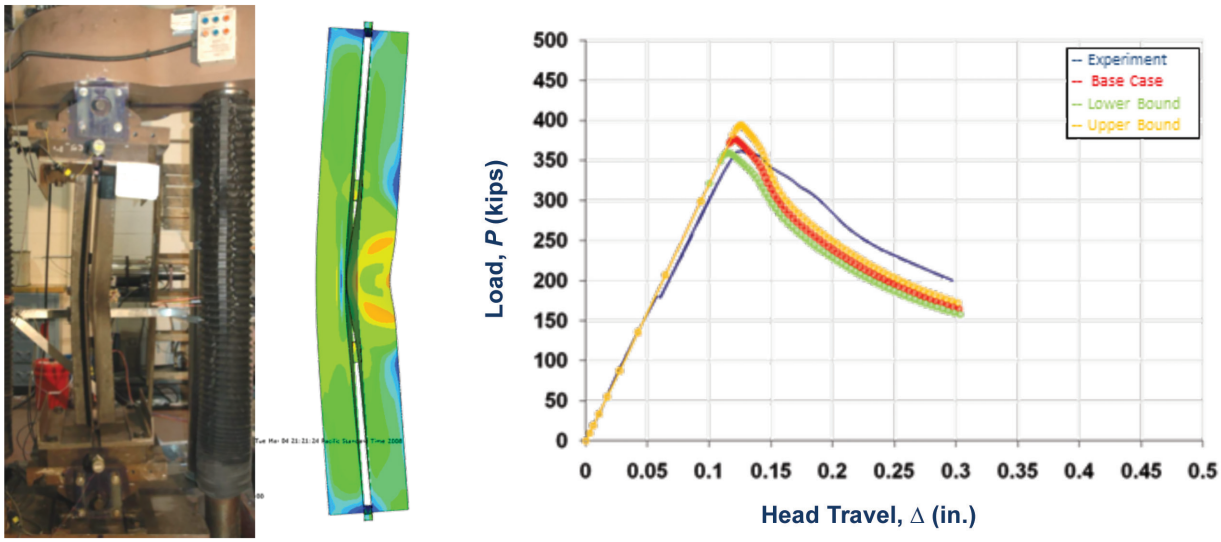


*(a) Experimental and analytical shape (showing von Mises stress)*

*(b) Load-displacement response (base case and stress-strain bounds)*

*Fig. 14. Experimental and analytical behavior of specimen DA22.*

- The sensitivity to stress-strain variability (Tables 5 and 9) is within 6% of the base case.
- The sensitivity to geometric imperfection magnitude increases with slenderness ratio. For single-angle specimens, the sensitivity to imperfection magnitude is higher for the more slender SB specimens than SA specimens (Tables 6 and 7). For double-angle specimens, the sensitivity is highest for the more slender DC specimens than it is for the less slender DB and DA specimens, respectively (Tables 10 and 11).
- Using geometric imperfection magnitudes of $L/1500$ shows better correlation, and agrees with laboratory measurements (Tables 6, 7, 10, and 11).
- Generating geometric imperfections using mode shapes within $2F_b$ and $L/500$ magnitude consistently underpredicts the strength (Tables 6, 7, 10, and 11). The use of $2F_b$ is not recommended.
- Comparing the corresponding ratios in Tables 6 and 7 (single angles) and in Tables 10 and 11 (double angles), the sensitivity to mode shape combination weighting method is within 4%, with smaller differences for imperfection magnitudes of $L/1500$.
- The sensitivity to increasing the number of mode shapes from within $5F_b$ to $10F_b$ is within 5% (Tables 6, 7, 10, and 11). This sensitivity is smaller when using inversely proportional weights, which may enable the use of fewer mode shapes with more reliability.

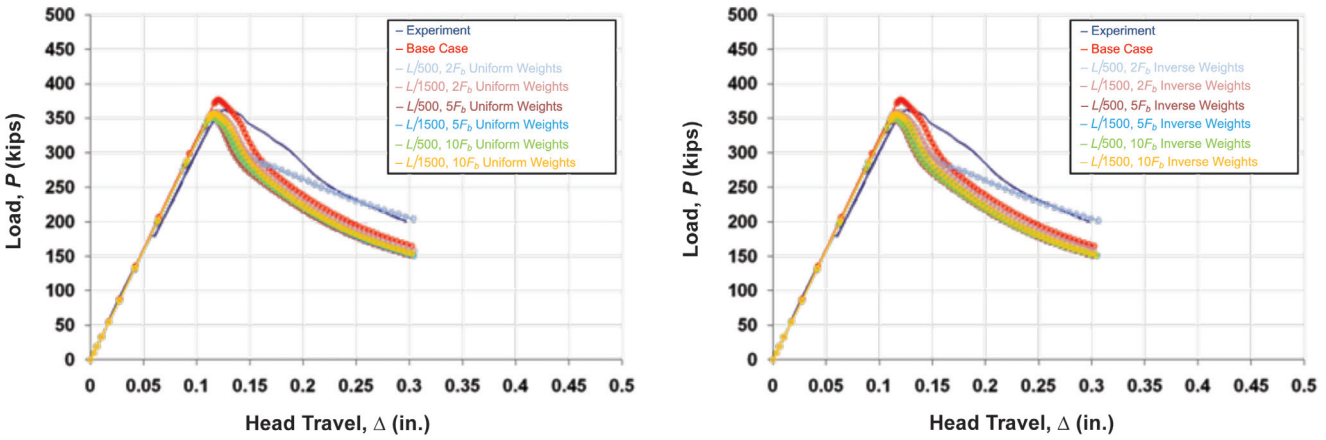


*(a) Uniformly weighted mode shapes* *(b) Inversely weighted mode shapes*

*Fig. 15. Effect of analytically generated imperfections on specimen DA22 buckling response.*

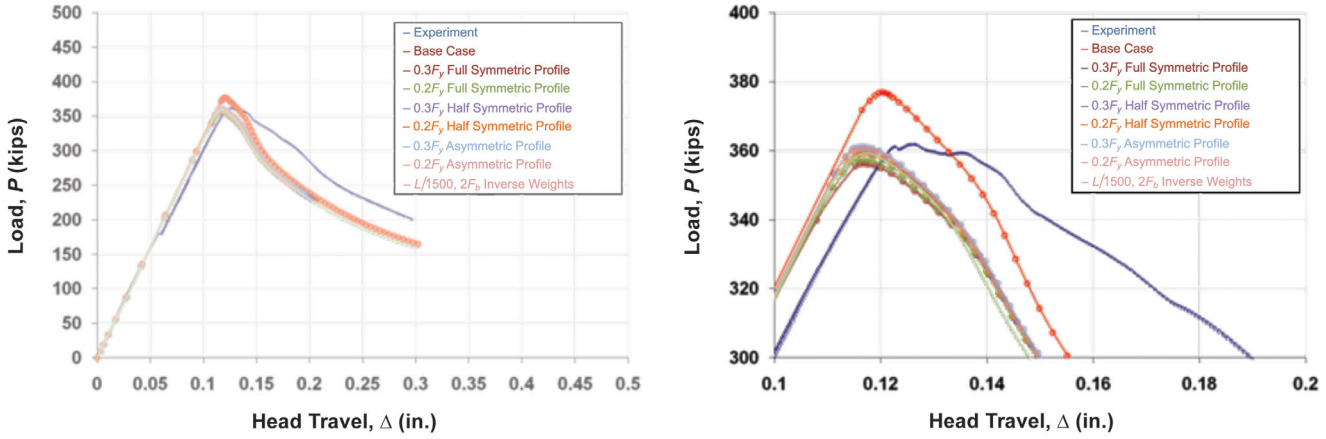


*(a) Full response* *(b) Close-up at peak response*

*Fig. 16. Effect of residual stresses on specimen DA22 buckling response.*

| Table 5. Analytical Single-Angle Buckling Strength and Effect of Stress-Strain Variability | | | | | | | |
|---|---|---|---|---|---|---|---|
| | Buckling Load (kips) | | | | | | |
| Specimen ID | $P_{exp}$ | Base $P$ | $P/P_{exp}$ | Upper-Bound $P$ | $P/P_{exp}$ | Lower-Bound $P$ | $P/P_{exp}$ |
| SA1 | 188 | 190 | 1.01 | 200 | 1.06 | 181 | 0.96 |
| SA2 | 162 | 180 | 1.11 | 188 | 1.16 | 173 | 1.06 |
| SA3 | 159 | 170 | 1.07 | 178 | 1.12 | 161 | 1.01 |
| Mean for SA | | | 1.06 | | 1.11 | | 1.01 |
| SB1 | 67.7 | 62.2 | 0.92 | 63.3 | 0.94 | 61.3 | 0.91 |
| SB4 | 56.6 | 48.9 | 0.86 | 49.2 | 0.87 | 48.6 | 0.86 |
| SB5 | 55.9 | 54.6 | 0.98 | 54.9 | 0.98 | 54.2 | 0.97 |
| Mean for SB | | | 0.92 | | 0.93 | | 0.91 |
| Overall mean | | | 0.99 | | 1.02 | | 0.96 |

| Table 6. Summary of Single-Angle Analytically Generated Geometric Imperfections with Uniform Weights | | | | | | | | | | | | |
|---|---|---|---|---|---|---|---|---|---|---|---|---|
| Specimen | SA | | | | SB | | | | All | | | |
| | $P_{case}/P_{base}$ | | | | $P_{case}/P_{base}$ | | | | $P_{case}/P_{base}$ | | | |
| Case[a,b] | Avg | Std | Max | Min | Avg | Std | Max | Min | Avg | Std | Max | Min |
| $5F_b$, $L/500$ | 0.99 | 0.01 | 0.99 | 0.98 | 0.96 | 0.03 | 0.99 | 0.94 | 0.98 | 0.02 | 0.99 | 0.94 |
| $10F_b$, $L/500$ | 0.98 | 0.02 | 1.00 | 0.96 | 0.97 | 0.03 | 0.99 | 0.94 | 0.98 | 0.02 | 1.00 | 0.94 |
| $5F_b$, $L/1500$ | 1.01 | 0.02 | 1.03 | 1.00 | 1.00 | 0.01 | 1.01 | 0.99 | 1.01 | 0.01 | 1.03 | 0.99 |
| $10F_b$, $L/1500$ | 1.01 | 0.01 | 1.02 | 1.00 | 1.03 | 0.05 | 1.09 | 0.99 | 1.02 | 0.04 | 1.09 | 0.99 |
| | $P_{base}/P_{exp}$ | | | | $P_{base}/P_{exp}$ | | | | $P_{base}/P_{exp}$ | | | |
| | Avg | Std | Max | Min | Avg | Std | Max | Min | Avg | Std | Max | Min |
| Base case | 1.06 | 0.05 | 1.11 | 1.01 | 0.92 | 0.06 | 0.98 | 0.86 | 0.99 | 0.09 | 1.11 | 0.86 |

[a] $F_b$ refers to first-mode elastic buckling load based on perfect geometry.
[b] The $2F_b$ cases were not implemented for uniformly weighted mode shapes.

| Table 7. Summary of Single-Angle Analytically Generated Geometric Imperfections Combined with Inverse Weights | | | | | | | | | | | | |
|---|---|---|---|---|---|---|---|---|---|---|---|---|
| Specimen | SA | | | | SB | | | | All | | | |
| | $P_{case}/P_{base}$ | | | | $P_{case}/P_{base}$ | | | | $P_{case}/P_{base}$ | | | |
| Case[a] | Avg | Std | Max | Min | Avg | Std | Max | Min | Avg | Std | Max | Min |
| $2F_b$, $L/500$ | 0.97 | 0.03 | 0.99 | 0.94 | 0.94 | 0.02 | 0.95 | 0.92 | 0.95 | 0.03 | 0.99 | 0.92 |
| $5F_b$, $L/500$ | 0.98 | 0.02 | 0.99 | 0.96 | 0.96 | 0.02 | 0.98 | 0.94 | 0.97 | 0.02 | 0.99 | 0.94 |
| $10F_b$, $L/500$ | 0.98 | 0.03 | 1.00 | 0.95 | 0.96 | 0.02 | 0.99 | 0.94 | 0.97 | 0.03 | 1.00 | 0.94 |
| $2F_b$, $L/1500$ | 1.01 | 0.01 | 1.01 | 1.00 | 0.97 | 0.03 | 0.98 | 0.94 | 0.99 | 0.03 | 1.01 | 0.94 |
| $5F_b$, $L/1500$ | 1.02 | 0.02 | 1.04 | 1.00 | 0.99 | 0.00 | 1.00 | 0.99 | 1.01 | 0.02 | 1.04 | 0.99 |
| $10F_b$, $L/1500$ | 1.02 | 0.02 | 1.04 | 1.00 | 0.99 | 0.01 | 1.00 | 0.99 | 1.01 | 0.02 | 1.04 | 0.99 |
| | $P_{base}/P_{exp}$ | | | | $P_{base}/P_{exp}$ | | | | $P_{base}/P_{exp}$ | | | |
| | Avg | Std | Max | Min | Avg | Std | Max | Min | Avg | Std | Max | Min |
| Base case | 1.06 | 0.05 | 1.11 | 1.01 | 0.92 | 0.06 | 0.98 | 0.86 | 0.99 | 0.09 | 1.11 | 0.86 |

[a] $F_b$ refers to first-mode elastic buckling load based on perfect geometry.

| Table 8. Summary of Single-Angle Effect of Residual Stresses | | | | | | | | | | | | |
|---|---|---|---|---|---|---|---|---|---|---|---|---|
| **Specimen** | **SA** | | | | **SB** | | | | **All** | | | |
| | $P_{case}/P_{cont}$ | | | | $P_{case}/P_{cont}$ | | | | $P_{case}/P_{cont}$ | | | |
| **Case**[a] | **Avg** | **Std** | **Max** | **Min** | **Avg** | **Std** | **Max** | **Min** | **Avg** | **Std** | **Max** | **Min** |
| Full symmetric $0.2F_y$ | 0.99 | 0.01 | 1.00 | 0.97 | 0.99 | 0.00 | 0.99 | 0.98 | 0.99 | 0.01 | 1.00 | 0.97 |
| Full symmetric $0.3F_y$ | 0.98 | 0.02 | 1.00 | 0.95 | 0.98 | 0.01 | 0.98 | 0.97 | 0.98 | 0.02 | 1.00 | 0.95 |
| Half symmetric $0.2F_y$ | 1.00 | 0.00 | 1.00 | 0.99 | 1.01 | 0.00 | 1.01 | 1.01 | 1.00 | 0.01 | 1.01 | 0.99 |
| Half symmetric $0.3F_y$ | 0.99 | 0.01 | 1.00 | 0.97 | 1.00 | 0.02 | 1.02 | 0.98 | 1.00 | 0.02 | 1.02 | 0.97 |
| Asymmetric (v) $0.2F_y$ | 1.00 | 0.00 | 1.00 | 0.99 | 1.02 | 0.01 | 1.03 | 1.02 | 1.01 | 0.01 | 1.03 | 0.99 |
| Asymmetric (v) $0.3F_y$ | 0.99 | 0.01 | 1.00 | 0.98 | 1.03 | 0.01 | 1.04 | 1.02 | 1.01 | 0.02 | 1.04 | 0.98 |
| | $P_{cont}/P_{exp}$ | | | | $P_{cont}/P_{exp}$ | | | | $P_{cont}/P_{exp}$ | | | |
| | **Avg** | **Std** | **Max** | **Min** | **Avg** | **Std** | **Max** | **Min** | **Avg** | **Std** | **Max** | **Min** |
| Control case[b] | 1.07 | 0.06 | 1.13 | 1.01 | 0.89 | 0.06 | 0.96 | 0.85 | 0.98 | 0.11 | 1.13 | 0.85 |

[a] Refer to Figure 13.
[b] Geometry set to inversely weighted mode shapes within twice the elastic buckling load with $L/1500$ imperfection magnitude.

| Table 9. Analytical Double-Angle Buckling Strength and Effect of Stress-Strain Variability | | | | | | | |
|---|---|---|---|---|---|---|---|
| | **Buckling Load (kips)** | | | | | | |
| **Specimen ID** | $P_{exp}$ | **Base** $P$ | $P/P_{exp}$ | **Upper-Bound** $P$ | $P/P_{exp}$ | **Lower-Bound** $P$ | $P/P_{exp}$ |
| DA1 | 361 | 406 | 1.12 | 426 | 1.18 | 385 | 1.07 |
| DA2 | 344 | 389 | 1.13 | 409 | 1.19 | 371 | 1.08 |
| DA3 | 342 | 395 | 1.16 | 413 | 1.21 | 376 | 1.10 |
| DA4 | 339 | 380 | 1.12 | 395 | 1.17 | 364 | 1.07 |
| DA5 | 314 | 315 | 1.00 | 331 | 1.05 | 299 | 0.95 |
| DA12 | 360 | 399 | 1.11 | 419 | 1.16 | 380 | 1.05 |
| DA22 | 362 | 377 | 1.04 | 394 | 1.09 | 359 | 0.99 |
| DA42 | 301 | 351 | 1.17 | 362 | 1.20 | 339 | 1.12 |
| Mean for DA | | | 1.11 | | 1.16 | | 1.05 |
| DB1 | 143 | 138 | 0.96 | 140 | 0.98 | 135 | 0.94 |
| DB2 | 127 | 114 | 0.90 | 116 | 0.91 | 113 | 0.89 |
| DB3 | 118 | 113 | 0.96 | 113 | 0.96 | 112 | 0.95 |
| DB4 | 86.2 | 90.1 | 1.05 | 90.1 | 1.05 | 90.1 | 1.05 |
| DB5 | 99.1 | 100 | 1.01 | 101 | 1.02 | 99.2 | 1.00 |
| Mean for DB | | | 0.98 | | 0.98 | | 0.97 |
| DC1 | 63.6 | 66.3 | 1.04 | 69.2 | 1.09 | 63.3 | 1.00 |
| DC2 | 58.4 | 62.8 | 1.07 | 64.2 | 1.10 | 60.1 | 1.03 |
| DC3 | 52.3 | 58.4 | 1.12 | 59.8 | 1.14 | 57.2 | 1.09 |
| DC4 | 47.9 | 51.2 | 1.07 | 51.6 | 1.08 | 50.7 | 1.06 |
| DC32 | 47.3 | 51.2 | 1.08 | 51.4 | 1.09 | 51.0 | 1.08 |
| DC42 | 42.5 | 48.0 | 1.13 | 48.0 | 1.13 | 48.0 | 1.13 |
| Mean for DC | | | 1.19 | | 1.11 | | 1.07 |
| Overall mean | | | 1.07 | | 1.09 | | 1.03 |

| Table 10. Summary of Double-Angle Analytically Generated Imperfections Combined with Uniform Weights | | | | | | | | | | | | | | | | |
|---|---|---|---|---|---|---|---|---|---|---|---|---|---|---|---|---|
| **Specimen** | **DA** | | | | **DB** | | | | **DC** | | | | **All** | | | |
| | $P_{case}/P_{base}$ | | | | $P_{case}/P_{base}$ | | | | $P_{case}/P_{base}$ | | | | $P_{case}/P_{base}$ | | | |
| **Case[a]** | **Avg** | **Std** | **Max** | **Min** | **Avg** | **Std** | **Max** | **Min** | **Avg** | **Std** | **Max** | **Min** | **Avg** | **Std** | **Max** | **Min** |
| $2F_b$, $L/500$ | 0.95 | 0.03 | 0.99 | 0.91 | 0.90 | 0.03 | 0.95 | 0.87 | 0.84 | 0.03 | 0.88 | 0.81 | 0.90 | 0.06 | 0.99 | 0.81 |
| $5F_b$, $L/500$ | 0.95 | 0.04 | 1.00 | 0.87 | 0.95 | 0.03 | 0.99 | 0.92 | 0.91 | 0.02 | 0.96 | 0.89 | 0.94 | 0.04 | 1.00 | 0.87 |
| $10F_b$, $L/500$ | 0.96 | 0.03 | 1.01 | 0.90 | 0.99 | 0.03 | 1.02 | 0.94 | 0.96 | 0.04 | 1.00 | 0.91 | 0.97 | 0.04 | 1.02 | 0.90 |
| $2F_b$, $L/1500$ | 1.00 | 0.03 | 1.06 | 0.95 | 0.95 | 0.02 | 0.99 | 0.93 | 0.94 | 0.04 | 1.00 | 0.91 | 0.97 | 0.04 | 1.06 | 0.91 |
| $5F_b$, $L/1500$ | 0.99 | 0.03 | 1.04 | 0.94 | 1.00 | 0.05 | 1.05 | 0.92 | 1.01 | 0.03 | 1.06 | 0.97 | 1.00 | 0.03 | 1.06 | 0.92 |
| $10F_b$, $L/1500$ | 1.00 | 0.03 | 1.05 | 0.94 | 1.01 | 0.05 | 1.06 | 0.93 | 1.02 | 0.04 | 1.08 | 0.98 | 1.01 | 0.04 | 1.08 | 0.93 |
| | $P_{base}/P_{exp}$ | | | | $P_{base}/P_{exp}$ | | | | $P_{base}/P_{exp}$ | | | | $P_{base}/P_{exp}$ | | | |
| | **Avg** | **Std** | **Max** | **Min** | **Avg** | **Std** | **Max** | **Min** | **Avg** | **Std** | **Max** | **Min** | **Avg** | **Std** | **Max** | **Min** |
| Base case | 1.11 | 0.06 | 1.17 | 1.00 | 0.97 | 0.06 | 1.05 | 0.90 | 1.09 | 0.03 | 1.13 | 1.04 | 1.07 | 0.07 | 1.17 | 0.90 |

[a] $F_b$ refers to first-mode elastic buckling load based on perfect geometry.

| Table 11. Summary of Double-Angle Analytically Generated Imperfections Combined with Inverse Weights | | | | | | | | | | | | | | | | |
|---|---|---|---|---|---|---|---|---|---|---|---|---|---|---|---|---|
| **Specimen** | **DA** | | | | **DB** | | | | **DC** | | | | **All** | | | |
| | $P_{case}/P_{base}$ | | | | $P_{case}/P_{base}$ | | | | $P_{case}/P_{base}$ | | | | $P_{case}/P_{base}$ | | | |
| **Case[a]** | **Avg** | **Std** | **Max** | **Min** | **Avg** | **Std** | **Max** | **Min** | **Avg** | **Std** | **Max** | **Min** | **Avg** | **Std** | **Max** | **Min** |
| $2F_b$, $L/500$ | 0.91 | 0.09 | 0.99 | 0.71 | 0.90 | 0.04 | 0.95 | 0.86 | 0.83 | 0.03 | 0.87 | 0.81 | 0.88 | 0.07 | 0.99 | 0.71 |
| $5F_b$, $L/500$ | 0.95 | 0.04 | 0.99 | 0.86 | 0.95 | 0.05 | 1.00 | 0.90 | 0.88 | 0.03 | 0.92 | 0.85 | 0.93 | 0.05 | 1.00 | 0.85 |
| $10F_b$, $L/500$ | 0.95 | 0.04 | 0.99 | 0.87 | 0.96 | 0.05 | 1.01 | 0.90 | 0.89 | 0.03 | 0.93 | 0.86 | 0.93 | 0.05 | 1.01 | 0.86 |
| $2F_b$, $L/1500$ | 0.99 | 0.05 | 1.04 | 0.90 | 0.94 | 0.03 | 0.98 | 0.92 | 0.93 | 0.04 | 0.99 | 0.90 | 0.96 | 0.04 | 1.04 | 0.90 |
| $5F_b$, $L/1500$ | 0.99 | 0.03 | 1.03 | 0.94 | 1.00 | 0.04 | 1.06 | 0.97 | 0.98 | 0.04 | 1.04 | 0.92 | 0.99 | 0.04 | 1.06 | 0.92 |
| $10F_b$, $L/1500$ | 1.00 | 0.03 | 1.03 | 0.94 | 1.01 | 0.04 | 1.06 | 0.97 | 0.99 | 0.04 | 1.05 | 0.92 | 1.00 | 0.04 | 1.06 | 0.92 |
| | $P_{base}/P_{exp}$ | | | | $P_{base}/P_{exp}$ | | | | $P_{base}/P_{exp}$ | | | | $P_{base}/P_{exp}$ | | | |
| | **Avg** | **Std** | **Max** | **Min** | **Avg** | **Std** | **Max** | **Min** | **Avg** | **Std** | **Max** | **Min** | **Avg** | **Std** | **Max** | **Min** |
| Base case | 1.11 | 0.06 | 1.17 | 1.00 | 0.97 | 0.06 | 1.05 | 0.90 | 1.09 | 0.03 | 1.13 | 1.04 | 1.07 | 0.07 | 1.17 | 0.90 |

[a] $F_b$ refers to first-mode elastic buckling load based on perfect geometry.

| Table 12. Summary of Double-Angle Effect of Residual Stresses | | | | | | | | | | | | | | | | |
|---|---|---|---|---|---|---|---|---|---|---|---|---|---|---|---|---|
| **Specimen** | **DA** | | | | **DB** | | | | **DC** | | | | **All** | | | |
| | $P_{case}/P_{cont}$ | | | | $P_{case}/P_{cont}$ | | | | $P_{case}/P_{cont}$ | | | | $P_{case}/P_{cont}$ | | | |
| **Case[a]** | **Avg** | **Std** | **Max** | **Min** | **Avg** | **Std** | **Max** | **Min** | **Avg** | **Std** | **Max** | **Min** | **Avg** | **Std** | **Max** | **Min** |
| Full symmetric $0.2F_y$ | 0.99 | 0.01 | 1.00 | 0.97 | 0.98 | 0.01 | 1.00 | 0.97 | 0.95 | 0.01 | 0.96 | 0.94 | 0.97 | 0.02 | 1.00 | 0.94 |
| Full symmetric $0.3F_y$ | 0.98 | 0.02 | 1.00 | 0.95 | 0.98 | 0.01 | 0.99 | 0.96 | 0.94 | 0.01 | 0.96 | 0.92 | 0.97 | 0.02 | 1.00 | 0.92 |
| Half symmetric $0.2F_y$ | 1.00 | 0.00 | 1.00 | 0.99 | 1.00 | 0.01 | 1.02 | 0.99 | 0.96 | 0.02 | 1.00 | 0.95 | 0.99 | 0.02 | 1.02 | 0.95 |
| Half symmetric $0.3F_y$ | 1.00 | 0.01 | 1.00 | 0.99 | 1.00 | 0.01 | 1.01 | 0.99 | 0.96 | 0.02 | 1.00 | 0.95 | 0.99 | 0.02 | 1.01 | 0.95 |
| Asymmetric (v) $0.2F_y$ | 1.00 | 0.00 | 1.01 | 1.00 | 1.02 | 0.01 | 1.04 | 1.00 | 0.97 | 0.03 | 1.02 | 0.91 | 1.00 | 0.03 | 1.04 | 0.91 |
| Asymmetric (v) $0.3F_y$ | 1.00 | 0.01 | 1.01 | 1.00 | 1.01 | 0.01 | 1.03 | 1.00 | 0.97 | 0.02 | 1.01 | 0.96 | 1.00 | 0.02 | 1.03 | 0.96 |
| | $P_{cont}/P_{exp}$ | | | | $P_{cont}/P_{exp}$ | | | | $P_{cont}/P_{exp}$ | | | | $P_{cont}/P_{exp}$ | | | |
| | **Avg** | **Std** | **Max** | **Min** | **Avg** | **Std** | **Max** | **Min** | **Avg** | **Std** | **Max** | **Min** | **Avg** | **Std** | **Max** | **Min** |
| Control case[b] | 1.09 | 0.09 | 1.22 | 0.97 | 0.92 | 0.06 | 0.99 | 0.85 | 1.01 | 0.05 | 1.07 | 0.96 | 1.02 | 0.10 | 1.22 | 0.85 |

[a] Refer to Figure 13.
[b] Geometry set to inversely weighted mode shapes within twice the elastic buckling load with $L/1500$ imperfection magnitude.

- The sensitivity to residual stress in Tables 8 and 12 is within 5% except for the DC series (9%), which has smallest cross-section size (LL1¾×1¾×⅛).
- The full symmetric residual stress profile consistently predicts buckling capacities lower than the control cases in Tables 8 and 12. The other two residual stress profiles predict buckling capacities both lower than and higher than the control cases.

## COMPUTATIONAL SIMULATION OF TRUSS SUBASSEMBLIES

### FE Model Description

Shell elements are used in the FE models to represent the steel angles used for the chords, the web, and the web spacers, as well as the end gusset plates [Figure 17(a)]. Welds were modeled using nodal degrees of freedom (DOF) constraints between elements along the weld length. The model used multipoint constraints to link the nodes in contact with the end clevises to a master node at the center of the hole in the corresponding gusset plates. A preliminary mesh sensitivity study considered mesh sizes of 4, 8, and 12 rows of quadrilateral shell elements per angle leg. The difference in estimated buckling loads was within 1% among the three cases. Hence, a typical mesh of four rows of elements per angle leg was used. Near joint locations, the chord member mesh was refined to eight rows of elements per leg. A linear DOF constraint was imposed between nodes along the transition line from four to eight element rows. Where diagonal and chord members intersected, an irregular mesh of smaller element size was used to capture the stress and deformations occurring within the connection [Figure 17(b)].

An initial imperfection profile was assigned by superposing a number of buckling mode shapes as previously described, using uniform weights. The number of modes to include was selected to constitute a "complete set" whose buckling mode shape deformations are not biased toward any portion or panel(s) of the structure. Such a mode shape set is usually characterized by a noticeable shift in the elastic buckling load following the addition of a group of closely spaced buckling modes. Five values of maximum imperfection magnitudes were explored: 0.05, 0.075, 0.10, 0.20, and 0.40 in.

The loading sequence consisted of self-weight, followed by proportional loading at the end clevises up to the displacement level recorded in the laboratory. Specimens C4 and C5 were unloaded gradually, then proportionally loaded in the opposite direction. The Modified Riks algorithm was used in the analyses (ABAQUS, 2007). The base case analyses considered the stiffness of the loading girder and out-of-plane bracing to be effectively rigid. The sensitivity to this assumption was investigated, as discussed later.

For comparison of analytical and experimental behavior, the model in-plane and out-of-plane load-deflection responses and strain measurements were recorded at several points.

### Discussion of Results

The analytical load-displacement response is consistently stiffer than those observed in the laboratory experiments.

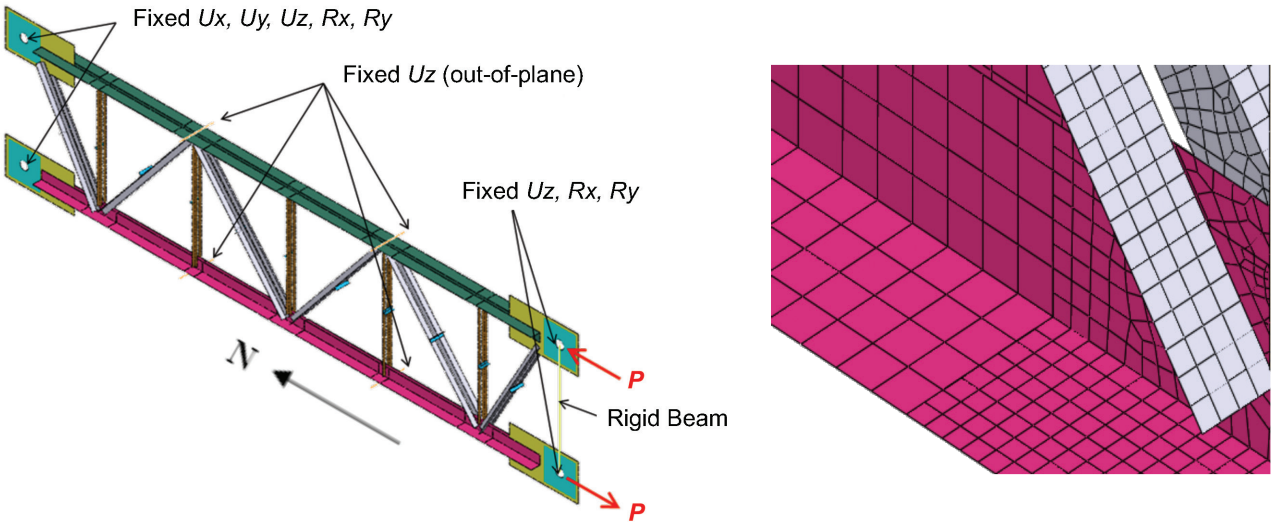


*(a) Geometry and boundary conditions (base case)* *(b) Mesh transition at joint*

*Fig. 17. ABAQUS FE model geometry and mesh for truss subassembly C4.*

| Table 13. Compression Chord Load Capacity for CM Base Cases (kips) | | | | | | |
|---|---|---|---|---|---|---|
| | | FE Simulations with Maximum Geometric Imperfection (in.) | | | | |
| Specimen | Test | 0.05 | 0.075 | 0.10 | 0.20 | 0.40 |
| C1 | 308 | 347 | 344 | 342 | 330 | 305 |
| C2 | 268 | 332 | 327 | 322 | 303 | 269 |
| C3 | 350 | 350 | 347 | 346 | 337 | 316 |
| C4, Phase 1[a] | 332 | 346 | 343 | 339 | 329 | 302 |
| C5, Phase 1[a] | 341 | 351 | 349 | 347 | 336 | 304 |
| C4, Phase 3[a] | 334 | 344 | 340 | 336 | 314 | 277 |
| C5, Phase 3[a] | 347 | 350 | 349 | 347 | 332 | 299 |
| [a] Phase 1 and Phase 3 refer to loading regimes causing buckling in the West and East chords, respectively. | | | | | | |

This is attributed to fit-up tolerances of the actuators and elimination of initial gaps in the test setup during early loading. Figure 18(a) shows the analytical load-displacement response at the center of the clevis attached to the West chord for specimen C1. The experimental load capacity is bounded by the analytical capacities for imperfection magnitudes of 0.20 and 0.40 in (about 1/1000 to 1/500 of the truss length). Figure 18(b) and Figure 18(c) compare the experimental and analytical deformed shapes, respectively (shown for 0.40-in. geometric imperfection magnitude, which resulted in the closest match with the experimental load capacity). The comparison indicates a similar deformed shape, although it is mirror-imaged to buckle in the South panel instead of the North panel (the specimen is symmetric). The following observations are summarized from all specimens:

- All FE simulations for Phase 1 result in primary buckling of the West chord taking place in the South panel; in some cases, the buckling zone extends to the Center panel. The FE component buckling modes are out-of-plane (strong axis) combined with local plate buckling, except for specimen C2, which, as expected, exhibits in-plane (weak-axis) buckling in the Center and South panels.
- The Phase 1 experimental tests resulted in primary buckling taking place in the Center panel, with members buckling locally and out of plane, except for two specimens: C1, where premature gusset plate rotation at the North clevis resulted in buckling initiating in the North panel before the Center panel, and C2, where the absence of vertical web members resulted in members buckling in-plane in the Center and South panels.
- The FE deformed shapes for Phase 3 have primary buckling at the East chord taking place in either the North panel (C4 specimen) or the South panel (C5 specimen), with buckling in both cases extending to the Center panel.
- The Phase 3 experimental test resulted in primary buckling in the Center panel of the East chord in both specimens C4 and C5.

The analytical maximum loads in the compression chord prior to buckling are compared to the test results in Table 13 for the range of maximum imperfections considered. The experimental load capacity is bounded by the FE simulation results, but the location of the buckling member is not always identical to the experiment. Except for specimen C3, all Phase 1 experimental load capacities fall within the bounds of the FE simulation results with 0.10- to 0.40-in. initial geometric imperfection magnitudes. The difference in analytical load capacity values between FE simulations of the different specimens increases with the magnitude of initial imperfection. In addition, the difference in load capacity from one specimen to another is larger in the experimental test results than in any of the FE simulations for any fixed value of assumed imperfection magnitude.

### Sensitivity to Loading Girder Stiffness

The loading setup in the CM specimen tests (Figure 10) is such that the loading girder has to undergo significant motion at its connections to the actuators, including both translation and rotation, in order to transfer the imposed displacement pattern on the clevises attached to the specimen at points P7 and P8. The deformation in the loading girder was ignored in the base cases. Consideration for finite stiffness of the loading girder has two main effects on the analytical response:

- The flexural flexibility of the loading girder affects the overall flexibility of the system and in particular the flexibility associated with the in-plane rotation of truss panels and chord members.
- The torsional flexibility of the loading girder affects the elastic buckling loads and mode shapes, introducing

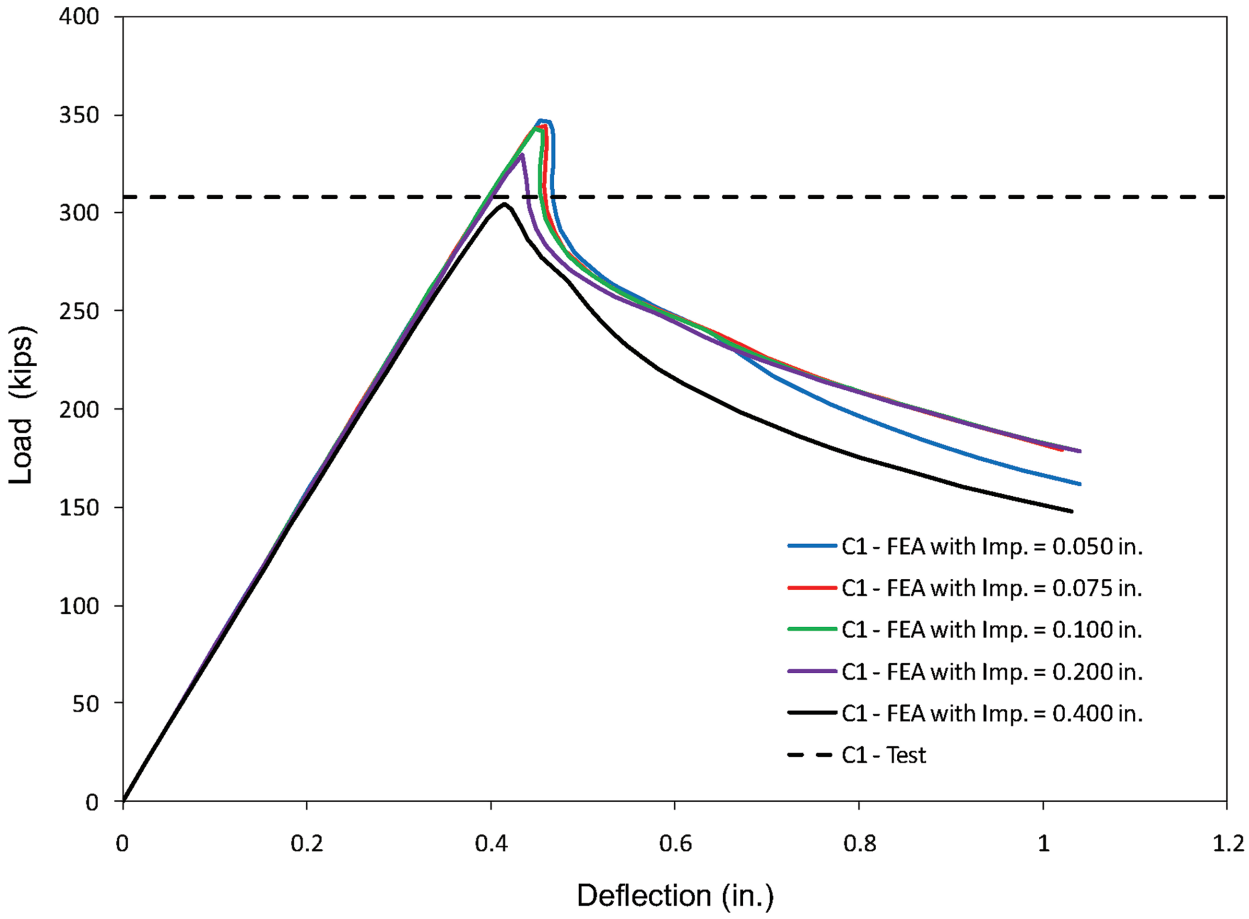


*(a) Load-axial shortening*

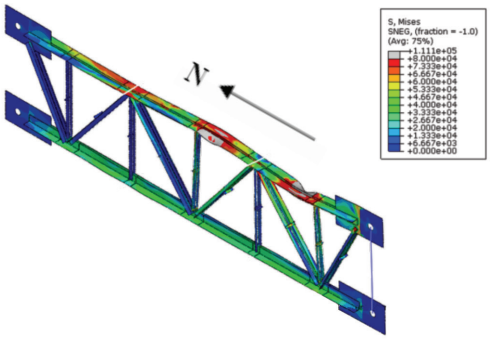


*(b) FE simulation (0.40-in. imperfection)*

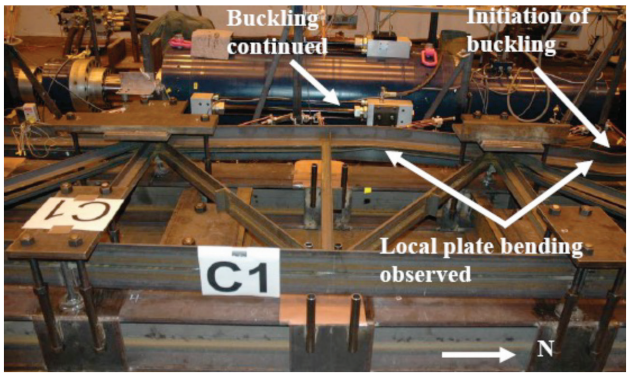


*(c) Test photo (West chord up)*

*Fig. 18. Analytical and experimental behavior capacity for specimen C1.*

two modes not previously observed with lower critical loads than the original first mode. These modes and the deformed shapes associated with their mode shapes when included in the calculation of initial geometric imperfection affect the initial geometry of the specimen in each simulation.

The behavior of the loading girder showed no evidence of nonlinearity throughout the experimental tests. Given the low span-to-depth ratio of the loading girder, six beam elements with shear-deformable (Timoshenko) formulation and a W30×326 cross section acting at the centerline of the loading girder were used between the actuator connection points, including two elements between P7 and P8. The boundary conditions are shown in Figure 19(a), where the out-of-plane translation of the loading girder at both ends and mid-span is restrained. The clevises were modeled using rigid offsets from the loading girder centerlines with allowance (release) for relative rotation at the clevis pin center. The modeled length of the loading girder is equal to the distance between the actuator axes. The loads at the ends of the loading girder were designated as follower loads so that they remain perpendicular to the girder. Only imperfection magnitudes of 0.10, 0.20, and 0.40 in. were considered.

Figure 19(b) shows the analytical deformed shape (with 0.4-in. initial geometric imperfection magnitude), which exhibits closer correlation to the experiment [Figure 18(c)] than the corresponding base-case simulation [Figure 18(b)]. Similar to the base case, the experimental load capacity is bounded by the analytical capacities for initial geometrical imperfection magnitudes of 0.20 and 0.40 in (Table 14). Including the loading girder stiffness in the FE models resulted in better correlation with the experimental results because the simulations correctly predicted the deformed shapes and buckling initiation for all five specimens. The analytical and experimental maximum loads are listed in Table 14 for all specimens. Comparison with Table 13 leads to the following observations:

- The modeling of loading girder stiffness results in a slight reduction in the estimated monotonic load capacity (Phase 1 loading).
- Except for specimen C3, all Phase 1 experimental load capacities fall within the bounds of the FE simulation results with 0.1- to 0.4-in. initial geometric imperfection magnitudes.
- In the base cases, analytical load capacities of Phase 3 loading were always lower than those of Phase 1 loading. Upon modeling the loading girder stiffness, Phase 3 estimated load capacities were higher than Phase 1 for specimen C4 and lower for C5. In the experimental results, load capacities for Phase 3 were slightly higher than Phase 1 for both specimens.

### Sensitivity to Out-of-Plane Bracing Stiffness

The out-of-plane bracing detail [Figure 10(c)] included initial gaps between the welded dowel and the bracing plates at each end, estimated at ⅛ in. combined between top and bottom sides. Under laboratory conditions, the self-weight and erection loads can close the initial gap on the lower side and increase the gap on the upper side. During loading, after contact between the welded dowel and the bracing system, the out-of-plane stiffness of the bracing system at

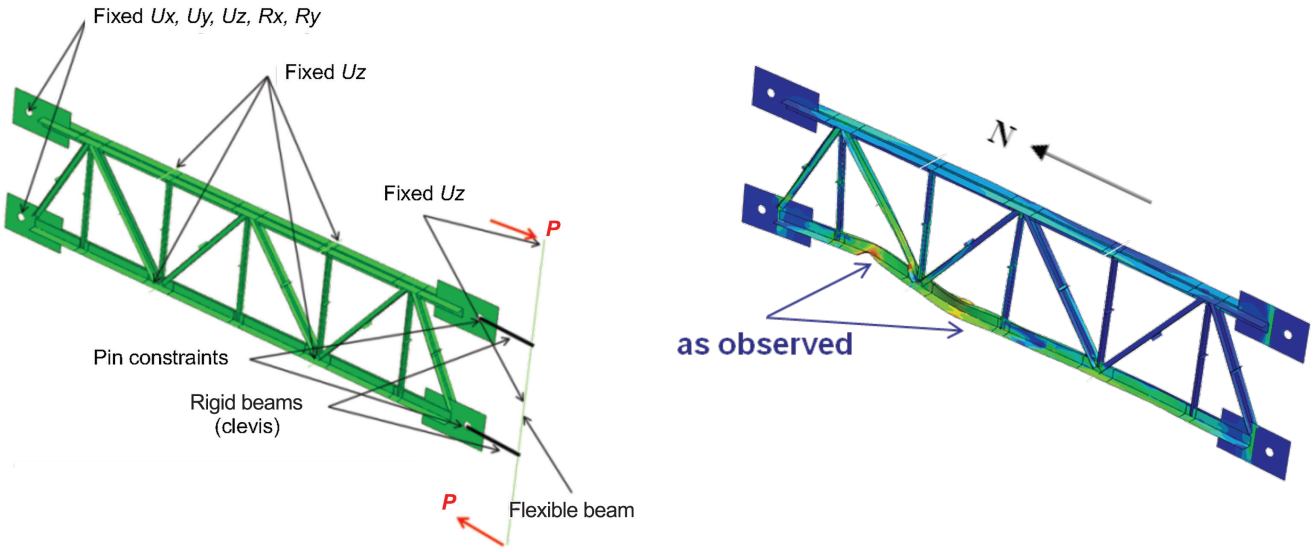


*(a) Boundary conditions* *(b) Deformed shape (West chord down)*

*Fig. 19. FE model and results for specimen C1 with flexible loading girder.*

| Table 14. Compression Chord Load Capacity for CM Flexible Girder Cases (kips) | | | | | | |
|---|---|---|---|---|---|---|
| | | FE Simulations with Maximum Geometric Imperfection (in.) | | | | |
| Specimen | Test | 0.05 | 0.075 | 0.10 | 0.20 | 0.40 |
| C1 | 308 | NA | NA | 335 | 321 | 291 |
| C2 | 268 | NA | NA | 312 | 292 | 254 |
| C3 | 350 | NA | NA | 338 | 323 | 296 |
| C4–Phase 1 | 332 | NA | NA | 336 | 324 | 305 |
| C5–Phase 1 | 341 | NA | NA | 343 | 335 | 316 |
| C4–Phase 3 | 334 | NA | NA | 337 | 339 | 328 |
| C5–Phase 3 | 347 | NA | NA | 340 | 332 | 312 |

the ends of the welded dowel is not symmetric. On the bottom side, the stiffness can be considered relatively infinite due to bearing on the pedestal beam, which, in turn, bears on the lab floor. On the top side, the stiffness is finite and can be derived as a series system composed of bending in the bracing plate and elongation in the four threaded rods. The plate bending stiffness was evaluated numerically as 1,430 kips/in., representative of a 20×6×1½ in. plate when loaded by a concentrated transverse load and supported at its four corners per the experimental setup. Threaded rod axial stiffness was calculated as 1,790 kips/in. The equivalent series system has a stiffness of 1,190 kips/in. for the bracing assembly. Nonlinear gap and contact elements were defined accordingly to simulate this bounding condition at the bracings.

The simulation of out-of-plane bracing stiffness included assigning the initial ⅛-in. gap as either split between top and bottom sides or all to the top side, in conjunction with multiple contact algorithms and solution control options. It was concluded that the inclusion of out-of-plane bracing stiffness did not significantly affect the analytical buckling load and yet had a significant negative effect on the solution time and numerical stability due to the contact iterations.

### Evaluation of Code Design Specifications

The AISC and SJI Specification equations for truss or joist member buckling are based on assumed end conditions for chord and web members and correspondingly assigned *K*-factors. In addition, the two Specification provisions provide no modification of the design loads to account for connection eccentricity in single-angle and double-angle member ends if the weld and member geometric centers do not coincide. For each subassembly specimen, the compression member strengths observed in the experiments (and determined using the FE simulations) were consistently higher than the ultimate strengths calculated using the Specification equations. This observation suggests that the effect of end conditions on the member behavior introduces more rotational fixity than is accounted for by the Specification equations. In other words, the experimental behavior corresponds to lower *K*-factors than the design equations specify, which result in a conservative design in these cases.

In order to evaluate this effect, Table 15 compares the experimental and Specification chord member buckling loads and computes the equivalent *K*-factor values, which correspond to the experimental buckling load. Chord member forces were calculated from the actuator forces using free-body equilibrium and linear geometric transformation. Chord member buckling lengths were defined between the panel working points. With the exception of specimens C1 (which experiences an unanticipated rotation in the gusset plate resulting in premature end-panel failure) and C2 (which experienced weak-axis buckling due to the absence of vertical web members), all the equivalent *K*-factors fall in the range 0.5 to 0.65. Table 15 is computed by assigning the appropriate *K*-factor using the 2010 SJI Specification based on the critical member bucking mode, end conditions, location, and structural role within the truss subassembly.

## SUMMARY

This study presents a procedure for analytically simulating the buckling behavior of single- and double-angle compression members and truss subassemblies and the performance of this procedure in comparison to experimental data. The members and subassemblies used in the experimental testing program were designed by the authors and the tests were performed at Lehigh University.

The single- and double-angle compression member correlation study was performed using FE simulations of 6 single-angle and 19 double-angle monotonic compression tests exhibiting buckling failure. For each specimen, the simulation consisted of a reference base case and an analytical sensitivity study matrix. The base case used measured angle dimensions and best-fit material properties from coupon tensile test results. The analytical sensitivity matrix included upper- and lower-bound material

| Table 15. Critical Chord Member Experimental and Predicted Buckling Strengths | | | | | |
|---|---|---|---|---|---|
| Specimen (Phase) | Buckling Location | Tested Strength (kips) | Predicted Strength (kips) | Design *K*-Factor[a] | Equivalent *K*-Factor |
| C1 | End panel | 308 | 308 | 1 | 1.00 |
| C2 | End panel | 268 | 258 | 1 | 0.94 |
| C3 | Middle panel | 350 | 298 | 1 | <0.50 |
| C4, Phase 1 | Middle panel | 332 | 298 | 1 | 0.65 |
| C4, Phase 3 | Middle panel | 334 | 298 | 1 | 0.63 |
| C5, Phase 1 | Middle panel | 341 | 298 | 1 | 0.53 |
| C5, Phase 3 | Middle panel | 347 | 298 | 1 | <0.50 |

[a] SJI *K*-factors range from 0.75 to 1.0 depending on the member type and buckling mode. Reported design *K*-factor corresponds to the member type and buckling mode observed during the test.

properties, several superposition procedures to generate geometric imperfections, two maximum geometric imperfection magnitudes, three residual stress profiles, and two maximum residual stress magnitudes.

The correlation study leads to the following conclusions regarding angle member buckling simulations:

- The sensitivity of buckling load to small variations in modeled stress-strain response is minor (less than 6%).
- The sensitivity of buckling load to residual stress inclusion is minor (less than 5%) except in small cross sections (up to 10%).
- The full symmetric residual stress profile is consistently conservative and thus appropriate for design applications.
- An out-of-straightness imperfection magnitude of $L/1500$ is appropriate for use with the experimental results.
- The generation of imperfection shapes based on elastic buckling mode shapes within 5 to 10 times the first-mode elastic buckling load produces stable results, with minor sensitivity to the combination method.

Based on these findings, the following recommendations are made for modeling buckling in steel single- and double-angle compression members:

- Using a material stress-strain response curve determined by curve-fitting several representative coupon test results is sufficient; minor variations may be ignored.
- Residual stress effects need only be considered for relatively small cross sections (L1¾×1¾×⅛ or smaller), based on the full-symmetric residual stress profile.
- Initial geometric imperfection shapes should be analytically generated using inversely weighted mode shapes within five times the lowest elastic buckling load and $L/1500$ magnitude.

The truss subassembly correlation study was performed using FE simulations of five double-angle truss subassemblies subjected to a constant moment couple loading (three monotonic, two cyclic). The specimens were designed to investigate buckling in chord members under different detailing configurations. A base FE case was constructed using nominal properties and analytically generated initial imperfections with magnitudes ranging from 0.05 to 0.40 in. The base case used a rigid loading girder and rigid out-of-plane bracing at panel points. The study investigated the effect of explicitly modeling the loading girder stiffness using shear-deformable beams and of modeling the out-of-plane bracing stiffness using nonlinear gap and contact elements. The subassembly correlation study also investigated the effect of subassembly member end conditions on the axial load capacity by comparing experimental and FE simulation results to capacities calculated using the SJI Specification.

The truss subassembly simulations successfully bounded the experimental buckling capacities using initial geometric imperfection magnitudes between 0.10 and 0.40 in. and captured the effect of prior buckling on the subassembly capacities under reversed loading. In general, the analytical load-displacement response was stiffer than observed in the experiment.

The subassembly correlation study leads to the following conclusions:

- Explicitly including the flexibility of the in-plane loading girder resulted in correct predictions of the buckling location. Assuming a rigid loading girder sometimes resulted in inaccurate analytical buckling locations, yet the analytical buckling capacities were not significantly affected. Explicit modeling of in-plane boundary element stiffness should be considered to accurately capture the correct buckling location.

- Explicitly modeling the out-of-plane bracing stiffness did not affect the analytical capacity and resulted in longer simulation times and convergence difficulties.
- For end panels, the chord member end conditions resulted in effective *K*-factor values close to the SJI design values of 1.0.
- For intermediate panels, the chord member end conditions resulted in effective *K*-factor values ranging from 0.50 to 0.65 compared to SJI design values of 1.0 (i.e., these SJI design values are conservative).

## ACKNOWLEDGMENTS

The Army Research Laboratory (ARL) mission is to execute fundamental and applied research to provide the Army with the key technologies and analytical support necessary to assure supremacy in future land warfare. A long-term research project sponsored by ARL under Cooperative Agreement Number DAAD 19-03-2-0036 and executed by the Advanced Technology Institute (ATI), was initiated in 2003 to assess the impact of HSLA-V steels on a wide variety of different army applications that use steel. A long-span joist study was awarded to SGH under contract with ATI. The continued support of ATI and ARL is gratefully acknowledged.

## REFERENCES

ABAQUS (2007), *ABAQUS User's Manual,* Version 6.7, Dassault Systemes, R.I.

Adluri, S.M.R. and Madugula, M.K.S. (1996), "Flexural Buckling of Steel Angles: Experimental Investigation," *Journal of Structural Engineering*, ASCE, Vol. 122, No. 3.

AISC (2005), *Specification for Structural Steel Buildings*, ANSI/AISC 360-05, American Institute of Steel Construction, Chicago, Ill.

AISC (2010), *Specification for Structural Steel Buildings*, ANSI/AISC 360-10, American Institute of Steel Construction, Chicago, Ill.

AISC (2016), *Specification for Structural Steel Buildings*, ANSI/AISC 360-16, American Institute of Steel Construction, Chicago, Ill.

Candas, A.B., Sause, R. and Ricles, J.M. (2008), *Experimental Study on Buckling of Vanadium Steel Members with Single- or Double-Angle Cross-Sections*, Report No. 08-07, Lehigh University ATLSS Center, Bethlehem, Pa.

Galambos, T.V. (1998), *Guide to Stability Design Criteria for Metal Structures*, 5th Ed., John Wiley & Sons, Inc.

SGH (2011), *Correlation and Sensitivity Study on the Buckling of HSLA-V Steel in Single and Double Angle Members*, Project 047079, Simpson, Gumpertz & Heger Inc.

SGH (2012), *Parameter Study to Assess Modifications to the SJI Design Equations for HSLA-V Steels. Rev.1.*, Project 047079, Simpson, Gumpertz & Heger Inc.

SJI (2010), *Standard Specification for Longspan Steel Joists, LH-Series and Deep Longspan Steel Joists, DLH-Series*, ANSI/SJI-LH/DLH, Steel Joist Institute, Florence, S.C.

SJI (2020), *Standard Specification for K-Series, LH-Series, and DLH-Series Open Web Steel Joists and for Joist Girders,* ANSI/SJI 100, Steel Joist Institute, Florence, S.C.